Plant Physiology and Biochemistry 196 (2023) 759–773

Contents lists available at ScienceDirect

Plant Physiology and Biochemistry

journal homepage: www.elsevier.com/locate/plaphy

Insights into the substrate specificity, structure, and dynamics of plant histidinol-phosphate aminotransferase (HISN6)

Maria Rutkiewicz [a], Isabel Nogues [b], Wojciech Witek [a], Sebastiana Angelaccio [c], Roberto Contestabile [c], Milosz Ruszkowski [a,*]

[a] Department of Structural Biology of Eukaryotes, Institute of Bioorganic Chemistry, Polish Academy of Sciences, Poznan, Poland
[b] Research Institute on Terrestrial Ecosystems, National Research Council, Monterotondo Scalo, Rome, Italy
[c] Istituto Pasteur Italia-Fondazione Cenci Bolognetti, Dipartimento di Scienze Biochimiche "A. Rossi Fanelli", Sapienza Università di Roma, Rome, Italy

ARTICLE INFO

Keywords:
Enzyme features
Histidinol-phosphate aminotransferase
Conformational change
Inhibition

ABSTRACT

Histidinol-phosphate aminotransferase is the sixth protein (hence HISN6) in the histidine biosynthetic pathway in plants. HISN6 is a pyridoxal 5′-phosphate (PLP)-dependent enzyme that catalyzes the reversible conversion of imidazole acetol phosphate into L-histidinol phosphate (HOLP). Here, we show that plant HISN6 enzymes are closely related to the orthologs from *Chloroflexota*. The studied example, HISN6 from *Medicago truncatula* (*Mt*HISN6), exhibits a surprisingly high affinity for HOLP, which is much higher than reported for bacterial homologs. Moreover, unlike the latter, *Mt*HISN6 does not transaminate phenylalanine. High-resolution crystal structures of *Mt*HISN6 in the open and closed states, as well as the complex with HOLP and the apo structure without PLP, bring new insights into the enzyme dynamics, pointing at a particular role of a string-like fragment that oscillates near the active site and participates in the HOLP binding. When *Mt*HISN6 is compared to bacterial orthologs with known structures, significant differences arise in or near the string region. The high affinity of *Mt*HISN6 appears linked to the particularly tight active site cavity. Finally, a virtual screening against a library of over 1.3 mln compounds revealed three sites in the *Mt*HISN6 structure with the potential to bind small molecules. Such compounds could be developed into herbicides inhibiting plant HISN6 enzymes absent in animals, which makes them a potential target for weed control agents.

1. Introduction

The cultivation of plant species important to agriculture depends on protection from weeds and pests. Humans have developed many ways to stop weeds from overgrowing crop fields. A modern example is herbicides, which are biologically-active chemical compounds that disturb weed growth and development through various modes of action. However, widespread herbicide usage has led to herbicide resistance (HR) in many weed species. The past six decades have brought more than 260 weed species resistant to over 160 herbicides due to their repeated use (Gould et al., 2018; Beckie et al., 2021; Gaines et al., 2021). Hence, we desperately need new herbicides to secure efficient agriculture and feed nearly eight billion people sustainably.

The most commonly used herbicide, glyphosate, inhibits 5-*enol*-pyruvyl-shikimate-3-phosphate synthase (EPSPS, EC 2.5.1.19) (Duke, 2018). EPSPS catalyzes the sixth step of the shikimate pathway that yields aromatic amino acids, *i.e.*, L-tryptophan (Trp), L-phenylalanine (Phe), and L-tyrosine (Tyr) (Maeda and Dudareva, 2012). For a long time, glyphosate was considered environmentally friendly because soil microflora can degrade it to CO_2, ammonia, and inorganic phosphate (P_i) (Forlani et al., 1999). Unfortunately, more and more weed species have developed resistance to glyphosate. Moreover, in 2015 the World Health Organization (WHO) announced that glyphosate might be carcinogenic according to the assessment by the International Agency for Research on Cancer (IARC) (Guyton et al., 2015). Despite the WHO declaration, in 2018, eighteen countries of the European Union renewed licenses for glyphosate use for the next five years. Recent findings have also demonstrated that glyphosate negatively affects pollinators, harming their cognitive and sensory abilities, thermoregulation, and gut microbiome (Motta et al., 2018; Farina et al., 2019; Vazquez et al., 2020; Weidenmuller et al., 2022). Therefore, searching for new herbicides and targets is now a high priority that should be conducted in parallel to the research on herbicide side effects.

The inhibition of the L-histidine (hereafter histidine) biosynthetic

* Corresponding author.
E-mail address: mruszkowski@ibch.poznan.pl (M. Ruszkowski).

https://doi.org/10.1016/j.plaphy.2023.02.017
Received 9 November 2022; Received in revised form 1 February 2023; Accepted 8 February 2023
Available online 10 February 2023

pathway (HBP) in plants is one of the promising solutions. The rationale behind targeting the HBP is threefold: (i) it occurs in prokaryotes, fungi, and plants but is absent in animals, (ii) loss-of-function mutants are lethal (Mo et al., 2006; Muralla et al., 2007), and (iii) most enzymes in the HBP are encoded by single genes (Stepansky and Leustek, 2006). The HBP is also integrated with other metabolic pathways, e.g., biosynthesis of nucleotides, other amino acids, and folates. All that suggests that inhibition of the HBP will disturb vital cellular processes directly by histidine depletion and indirectly by perturbing other metabolic pathways.

The plant HBP consists of eleven reactions catalyzed by eight enzymes named consecutively HISN1-8 that localize to the chloroplast stroma (Stepansky and Leustek, 2006). This article focuses on the HISN6 enzyme, which functionally is an L-histidinol phosphate aminotransferase (HAT) (EC 2.6.1.9). HISN6 is a pyridoxal 5′-phosphate (PLP)-dependent enzyme, classified into the Iβ subfamily (Jensen and Gu, 1996). It reversibly catalyzes the seventh step of the HBP; the interconversion of imidazole acetol phosphate (IAP) to L-histidinol phosphate (HOLP). The reaction is concomitant with the conversion of equimolar amounts of L-glutamate into 2-oxoglutarate (2OG) for the formation of pyridoxamine 5′-phosphate (PMP) (Haruyama et al., 2001; Fernandez et al., 2004) (Fig. 1).

In *Arabidopsis thaliana*, the knockout of the *AtHPA1* gene (encoding the *At*HISN6A enzyme) is embryo-lethal (Mo et al., 2006). Interestingly, the effect was not due to His starvation, but it made the plants unable to sustain primary root growth 2 days after germination. The exact role of *AtHPA1* in His signaling mechanisms in plants is yet to be understood. However, *A. thaliana* is one of the unique plant species that has the second (HISN6B) isoform, possibly able to take over in the HBP.

This article is a part of a series that provides experimental structures of plant HBP enzymes; the structures of HISN1 (Ruszkowski, 2018), HISN2 (Witek et al., 2021), HISN7 (Ruszkowski and Dauter, 2016), and HISN8 (Ruszkowski and Dauter, 2017) were published by us, and that of HISN5 by others (Glynn et al., 2005). Until now, our comprehension of plant HISN6 enzymes has been limited to what can be deduced from structures of bacterial homologs, as the structures were unavailable for any plant species. Here, we report a study of the structure and function of HISN6 from the model legume plant *Medicago truncatula* (*Mt*HISN6). We traced the evolution of the plant HISN6 enzymes and showed that they have evolved toward higher selectivity than bacterial homologs. We also compared *Mt*HISN6 with homologous structures from prokaryotes. We analyzed the closed and open forms of the *Mt*HISN6 structure, which vary by the positioning of a dynamic segment that either restricts or provides access to the active site. Finally, we determined the potential target regions for designing novel inhibitors of plant HISN6 that could be exploited in the herbicide design.

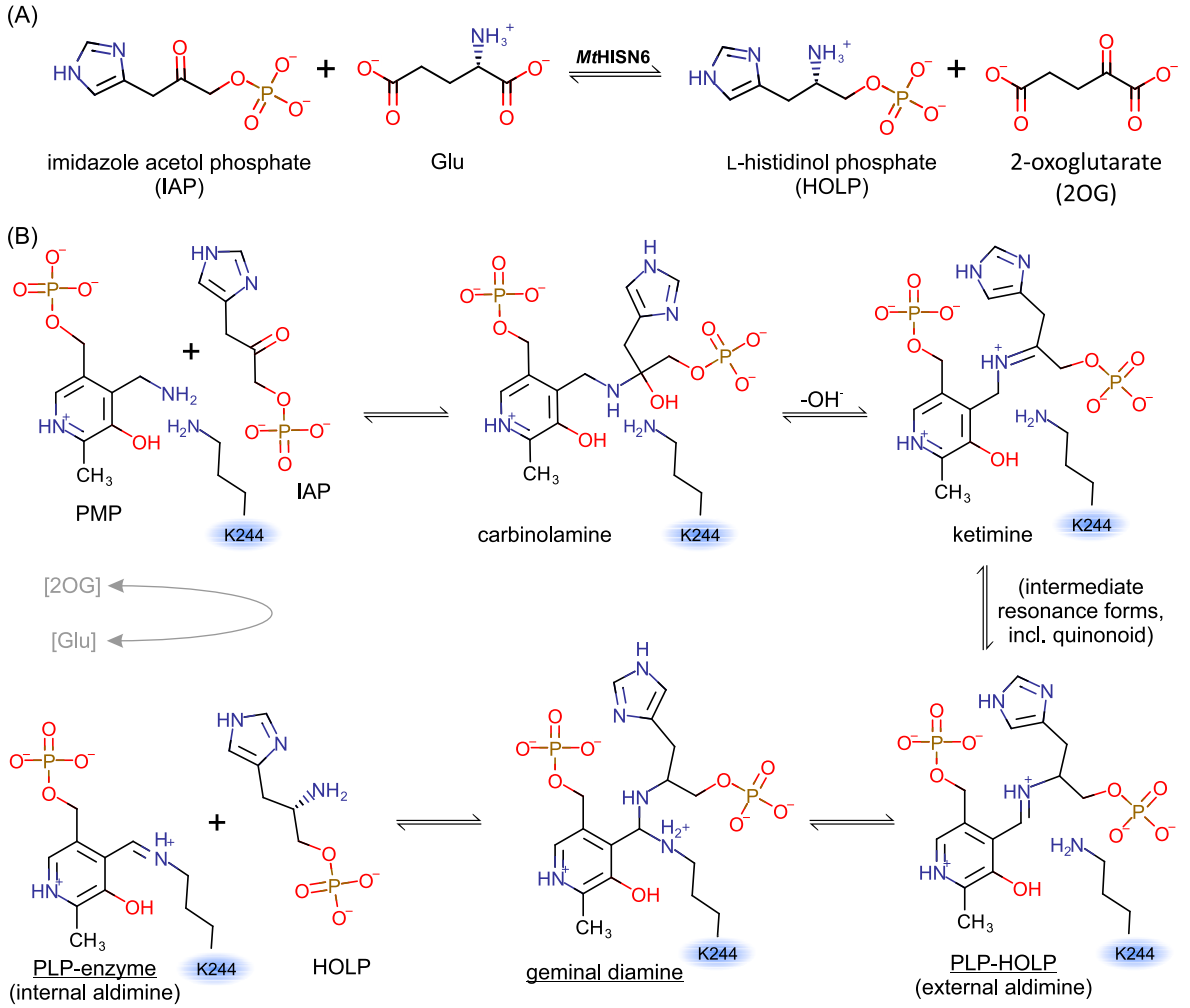

Fig. 1. (A) Simplified scheme of the reaction catalyzed by HISN6. The amino group is transferred from glutamate to imidazole acetol phosphate (IAP), creating histidinol phosphate (HOLP) and 2-oxoglutarate products. (B) The catalytic mechanism of the transamination reaction in the direction of the histidine biosynthetic pathway. Snapshots captured in this work crystal structures are underlined. The second half-reaction, *i.e.*, recharging PMP by glutamate, is indicated in gray.

2. Results

2.1. Evolution of plant HISN6 enzymes

Structural similarity network (SSN) analysis was conducted using 21,142 UniRef90 (Suzek et al., 2015) sequences from the InterPro (Blum et al., 2021) family of L-histidinol phosphate aminotransferases (IPR005861). The study revealed the scattered origin of bacterial HATs. *Archaea* share little similarity with surrounding groups suggesting that their HATs might have evolved independently (Fig. 2). Although *Opisthokonta* (in this case, primarily fungi) seems to be separated, it has a few connections with the phylum of *Bacteroidetes*. HAT enzymes from *Bacteroidetes* were likely ancestral to orthologs found in *Oomycota* (water molds) and *Bacillariophyta* (diatoms). Interestingly, phototrophic *Viridiplantae* (land plants) and *Chlorophyta* (green algae) are closely related to the bacterial *Chloroflexota* phylum (previously referred to as *Chloroflexi*) (Oren and Garrity, 2021). Unlike most chloroplast proteins that evolved from *Cyanobacteria* (Raven and Allen, 2003), a gene encoding HISN6 in plants seems to have been acquired from *Chloroflexota* by a horizontal gene transfer (HGT) independently from chloroplasts formation that occurred by absorbing *Cyanobacteria* (Yuzawa et al., 2012).

2.2. Functional assays of MtHISN6

*Mt*HISN6 orthologs have been studied in other species, but no report regarding substrate specificity is available for any eukaryotic source. IAP is the HISN6 substrate in the HBP, but it is commercially unavailable. Therefore, we assayed *Mt*HISN6 in the reverse direction (with HOLP as substrate) in a coupled assay with bovine glutamate dehydrogenase (GDH), which allows measuring NADH formation at 340 nm. Others have used a similar approach (Nasir et al., 2016). It was astounding to observe that *Mt*HISN6 exhibits a relatively high affinity towards HOLP, as reflected by a low K_M value of 29 μM (Fig. 3), which is nearly 15-fold lower than the K_M of *Mycobacterium tuberculosis* HAT (Nasir et al., 2016).

Moreover, in contrast to *M. tuberculosis* HAT, *Mt*HISN6 shows no measurable activity with Phe (up to 25 mM). We then tested whether the external aldimine forms in the presence of 1 mM Phe. The absorbance at 355 nm increased slowly, with the rate $k = 1.6$ min^{-1} (Supplementary Fig. S1). Notably, in the same experimental setup, the external aldimine formation with HOLP was too quick to measure, suggesting this step is not limiting in our coupled assay. On the other hand, *Mt*HISN6 exhibits a low catalytic activity, at least in the HOLP → IAP direction, with a turnover rate (k_{cat}) of 4 min^{-1}.

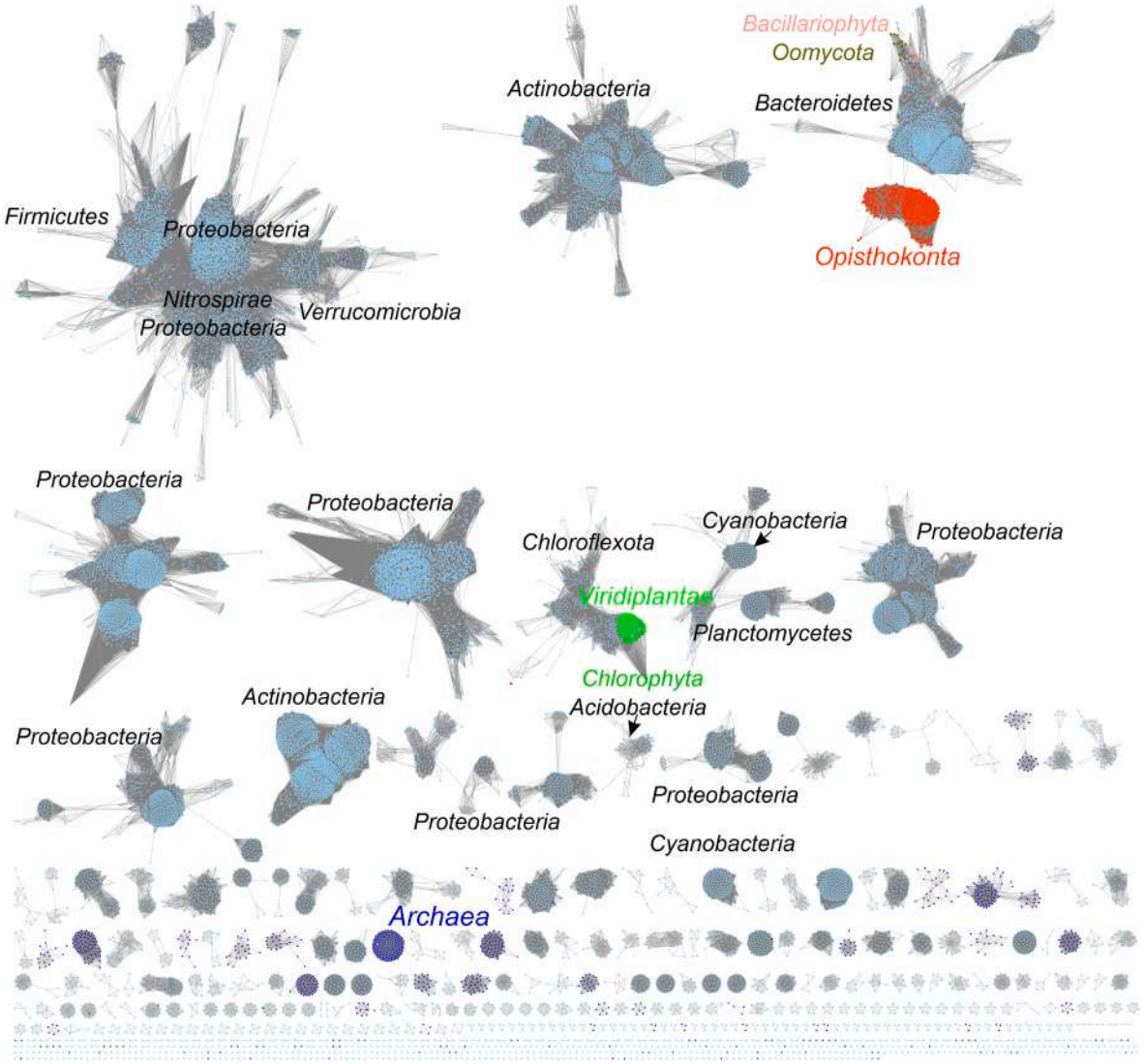

Fig. 2. Sequence similarity network of *Mt*HISN6 and its homologs. 21,142 UniRef90 clusters were analyzed. Higher plants (*Viridiplantae*) and green algae (*Chlorophyta*) are marked in green. Fungal sequences (*Opisthokonta*) are marked in red. Archaea are purple. Plant HISN6s group together with HATs from anoxygenic photoautotrophs, *Chloroflexota*.

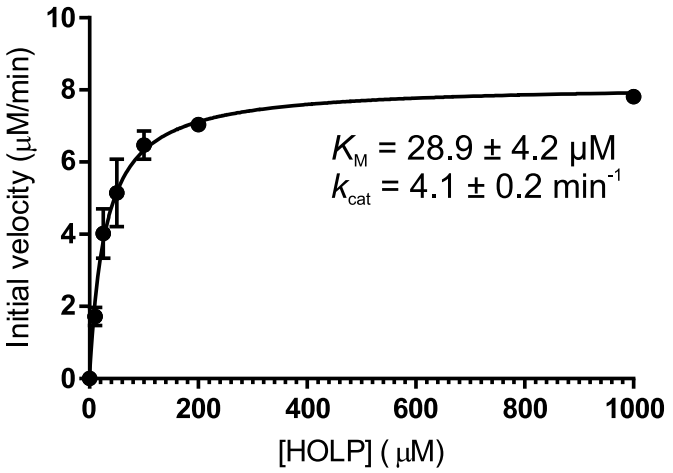

Fig. 3. Determination of kinetic parameters for the conversion of HOLP into IAP. The reaction was followed in a coupled assay as detailed in the text by monitoring the increase of NADH at 340 nm. Nonlinear least square analysis was used to fit the experimental data with the Michaelis-Menten equation, obtaining estimates of K_M and k_{cat}. Error bars on the average experimental points are standard deviations calculated from two independent replications.

2.3. Overall properties of the MtHISN6 structures

Crystal structures of *Mt*HISN6 were solved in the monoclinic space group, $P2_1$: (i) as a functional dimer in both open (1.57 Å resolution) and (ii) closed (1.40 Å) states and as (iii) a dimeric complex with HOLP (1.61 Å). The apo*Mt*HISN6 (without PLP, 1.45 Å) also crystallized in the $P2_1$ space group but with two dimers in the asymmetric unit (Table 1). The high-resolution electron density maps allowed us to trace residues from D25 until the C-termini (Fig. 4A). For the open conformation structure, the map for the I41-L47 fragment of chain B exhibits certain ambiguity, hinting at multiple possible conformations (one conformation was modeled). PLP in the active sites of closed and open forms of mature *Mt*HISN6 (with the PLP-prosthetic group) is bound as a Schiff-base to K244 (internal aldimine, Fig. 4B). The *Mt*HISN6_open model contains 842 water residues and buffer components, such as two surface-bound sodium ions (one per chain), fifteen 1,2-ethanediol molecules, and six sulfate ions. Two sulfate ions are located in each active site, while the remaining ones bind in small clefts (Fig. 4C). *Mt*HISN6_closed contains 1041 water residues and two acetate ions. Additionally, the map allowed us to model HEPES molecules (with partial occupancy) bound close to the dimer interface (Fig. 4D). The structure of the *Mt*HISN6-HOLP complex permitted the modeling of external aldimine in chain A and geminal diamine intermediate of HOLP in chain B; the side-chain conformations (except for K244) in the active sites are nearly identical. The model contains 823 water residues, two sodium ions, and eight 1,2-ethanediol molecules. Finally, the apo*Mt*HISN6 model was solved from crystals grown in ammonium sulfate but without adding an excess PLP. It contains 1413 water molecules, four sodium atoms, 12 sulfate ions, and 23 1,2-ethanediol molecules.

*Mt*HISN6 comprises the large (P72–N289) and the small domains (D25-P71, P290–S384), as per the terminology proposed by Ford et al. (1980) with modifications (Fig. 4A). The N-terminal part of the small domain is positioned in a shallow cleft on the dimer interface along the non-crystallographic 2-fold axis. It exists in two conformations: open and closed, which vary primarily by the positioning of the L35-P43 fragment that oscillates like a guitar string and the fragment F44–I58 containing two helices (Fig. 4B). The L35-P43 string is further from the active site in the open conformation, allowing the substrate to enter. Contrary, in the closed conformation, the L35-P43 string is drawn towards the active site entrance, restricting access and providing a proper environment for the catalysis. In the *Mt*HISN6-HOLP complex, which is also in the closed form, Y38 (from the string) H-bonds the substrate's phosphate oxygen and Nδ atoms (see below). Moreover, a minor rotation of the small domain in regard to the large domain occurs; the domains are closer in the *Mt*HISN6_closed structure (Fig. 4B).

The sodium cations are coordinated by the backbone carbonyls of K312, V314, and L317 (Fig. 4E). Furthermore, P315 imposes structural rigidity on the fragment, enforcing the positioning of the carbonyls to create the metal coordination sphere. Na^+ is bound to the same site in all ten subunits in this work structures, implying a specific binding relevant *in vivo*. This is a novelty, as previous structures of HATs from other sources did not contain metal cations except a magnesium ion bound to the *Geobacter metallireducens* HAT (Protein Data Bank, PDB, https://www.rcsb.org/; PDB ID: 3hdo, unpublished). However, in that case, the metal was bound at the crystal contact only in one of the two subunits. We cannot unambiguously state whether Na^+ binding is common in plant HISN6 enzymes with current data. However, the $_{312}$KAVPFL$_{317}$ fragment is similar in *Arabidopsis thaliana* HISN6A

Table 1
Data reduction and refinement statistics of MtHISN6 crystal structures. Values in parentheses are for the high resolution shell.

	*Mt*HISN6_open PDB ID: 8bj1	*Mt*HISN6_closed PDB ID: 8bj2	*Mt*HISN6_HOLP PDB ID: 8bj3	apo*Mt*HISN6 PDB ID: 8bj4
Diffraction source	APS 22-ID, Argonne, USA	APS 22-ID, Argonne, USA	APS 22-ID, Argonne, USA	P13 PETRA, Hamburg, Germany
Wavelength (Å)	1.0000	1.0000	1.0000	0.9763
Temperature (K)	100 K	100 K	100 K	100 K
Rotation range per image (°)	0.25	0.5	0.5	0.1
Total rotation range (°)	200	200	200	360
Space group	$P2_1$	$P2_1$	$P2_1$	$P2_1$
a, *b*, *c* (Å)	66.7, 87.4, 74.2	56.9, 105.8, 66.5	56.7, 66.3, 109.1	73.9, 93.0, 110.5
α, β, γ (°)	90, 95, 90	90, 108.9, 90	90, 106.5, 90	90, 73.5, 90
Mosaicity (°)	0.087	0.164	0.181	0.118
Resolution range (Å)	56.4–1.6 (1.66–1.57)	53.9–1.4 (1.48–1.40)	54.3–1.6 (1.71–1.61)	999.0–1.5 (1.54–1.45)
No. of unique reflections	116,740	145,641	97,979	252,775
Completeness (%)	98.6 (98.6)	99.2 (95.5)	99.5 (97.7)	99.6 (99.0)
Redundancy	3.9 (3.8)	4.0 (3.7)	4.1 (3.9)	6.77 (6.59)
I/σ(I)	18.02 (1.86)	13.89 (1.89)	18.61 (2.06)	13.71 (1.3)
R_{meas} (%)	5.2 (77.7)	5.8 (77.0)	5.8 (78.8)	8.6 (146.5)
CC1/2	99.9 (65.6)	99.9 (73.2)	99.9 (77.3)	99.9 (62.8)
Overall *B* factor: Wilson plot/all atoms (Å2)	20.8/28.3	16.8/21.3	19.2/22.1	18.5/26.5
No. of reflections: working/test set	116,740/1168	145,641/1164	97,979/1177	252,664/2527
R/ R_{free}	0.127/0.170	0.134/0.164	0.153/0.189	0.148/0.181
No. of non-H atoms: Protein/Ligand/Water	5936/92/887	5971/40/1087	5841/30/823	11,601/186/1630
R.m.s. deviations: Bonds (Å)/Angles (°)	0.008/1.011	0.008/0.930	0.008/0.920	0.008/0.944
Ramachandran plot: Most favored/allowed (%)	98.9/1.1	98.0/2.0	98.7/1.3	98.1/1.9

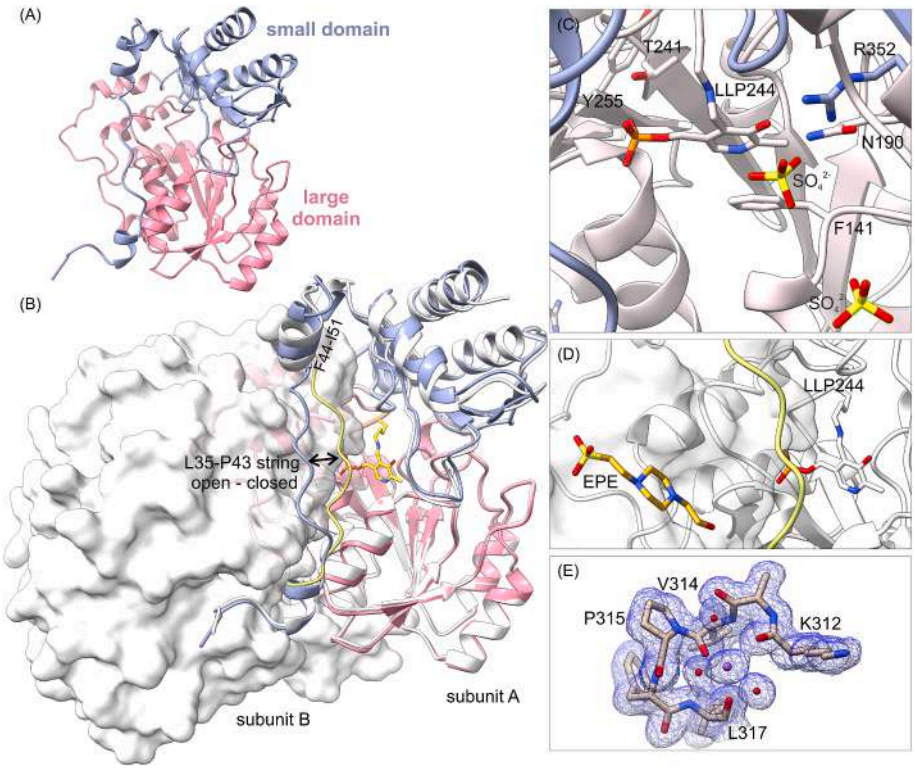

Fig. 4. Crystal structures of *Mt*HISN6 were determined in open and closed conformations. The most striking differences can be observed in the small domain, especially in the L35-P43 string. The subunit A of the open conformation structure is shown as a color-coded ribbon, where the small domain is blue and the large one is pink (A). (B) The dimer, where the subunit B is presented as a surface. *Mt*HISN6_closed is superimposed and shown as white ribbons, with the L35-P43 string colored green for easier identification. The stick representation of PLP bound in the form of internal aldimine marks the active site (B). The sulfate ions bind in the open conformation structure, mimicking the phosphate group of HOLP. Furthermore, two sulfate ions bind in small clefts between large and small domains (C). The buffer molecule, HEPES (EPE), binds on the dimer interface creating a steric hindrance to the string's opening (D). Panel E illustrates the Na^+ binding site; the 2Fo-Fc electron density map (blue mesh) is contoured at 1σ level.

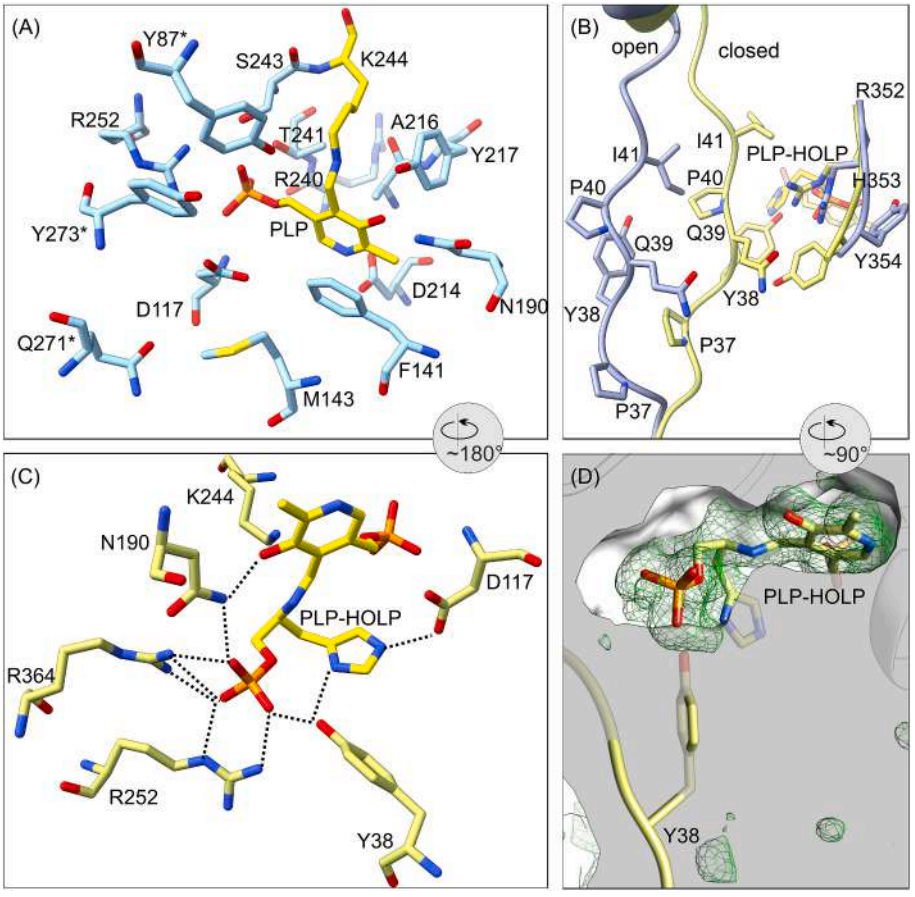

Fig. 5. The active site of *Mt*HISN6. PLP is bound in the form of internal aldimine creating a Schiff base. The side chains of residues constituting the active site are presented as sticks (A). (B) The movement of the string reduces the active site volume. The superposition of open (blue) and liganded (yellow) form structures shows how the closing of the loop restricts access to the active site. Binding of the ligand, HOLP, induces a conformational change of PLP, whose ring rotates by ~20° to attain position almost parallel to the phenyl ring of F141 (C). Panel D shows the Polder map (green mesh), contoured at 3σ level around PLP-HOLP. The protein surface is clipped to visualize the binding pocket.

(UniProt: B9DHD3; $_{345}$KEVPFL$_{350}$ sequence). Notwithstanding, the active site is > 20 Å away from Na^+, suggesting that the metal stabilizes the protein structure rather than directly participates in substrate binding or catalysis.

2.4. The active site of MtHISN6

The active site of *Mt*HISN6 contains a prosthetic group, PLP (Fig. 5A). PLP formed internal aldimines in our open and closed state structures, well defined by the electron density. The functional dimer has two active-site cavities located at the domain interface around the non-crystallographic 2-fold axis. Customarily, the residues forming the active site pocket are divided into bottom-forming and wall-forming ones (Haruyama et al., 2001). *Mt*HISN6 active site bottom consists of D117, F141, M143, N190, D214, A216, R240, Q271*, Y273* (asterisk denotes a residue from the dimer mate) whereas Y217, T241, S243, R252, and Y87* build the wall (Fig. 5A). Residues of the small domain, in particular P37, Y38, Q39, P40, and I41 (part of the movable string), make up a lid covering the active site (Fig. 5B).

PLP binds to the active site by forming an internal aldimine with K244 and an extensive net of non-covalent interactions. The PLP phosphate acts as an anchor by interacting with Y87*, S243, R252, and T241 side chains and A116-D117 main-chain amides. The methyl group of A216 and the phenyl ring of F141 sandwich the pyridine ring. The PLP N1 interacts with D214, whereas the hydroxy group, O3, is stabilized by Y217 (Oη) and N190 (Nδ, Fig. 5A). Two additional water-mediated H-bonds further stabilize PLP with respect to the residues at the bottom and side of the active center cavity: R364, D117, and Y87*.

The change from the open to the closed state reduces the size of the active site cavity, e.g., the distance between I41 Cα and H353 Cα decreases from 13.9 Å to 10.1 Å. This change is attained by moving the L35-P43 string, which restricts access to the active site cavity

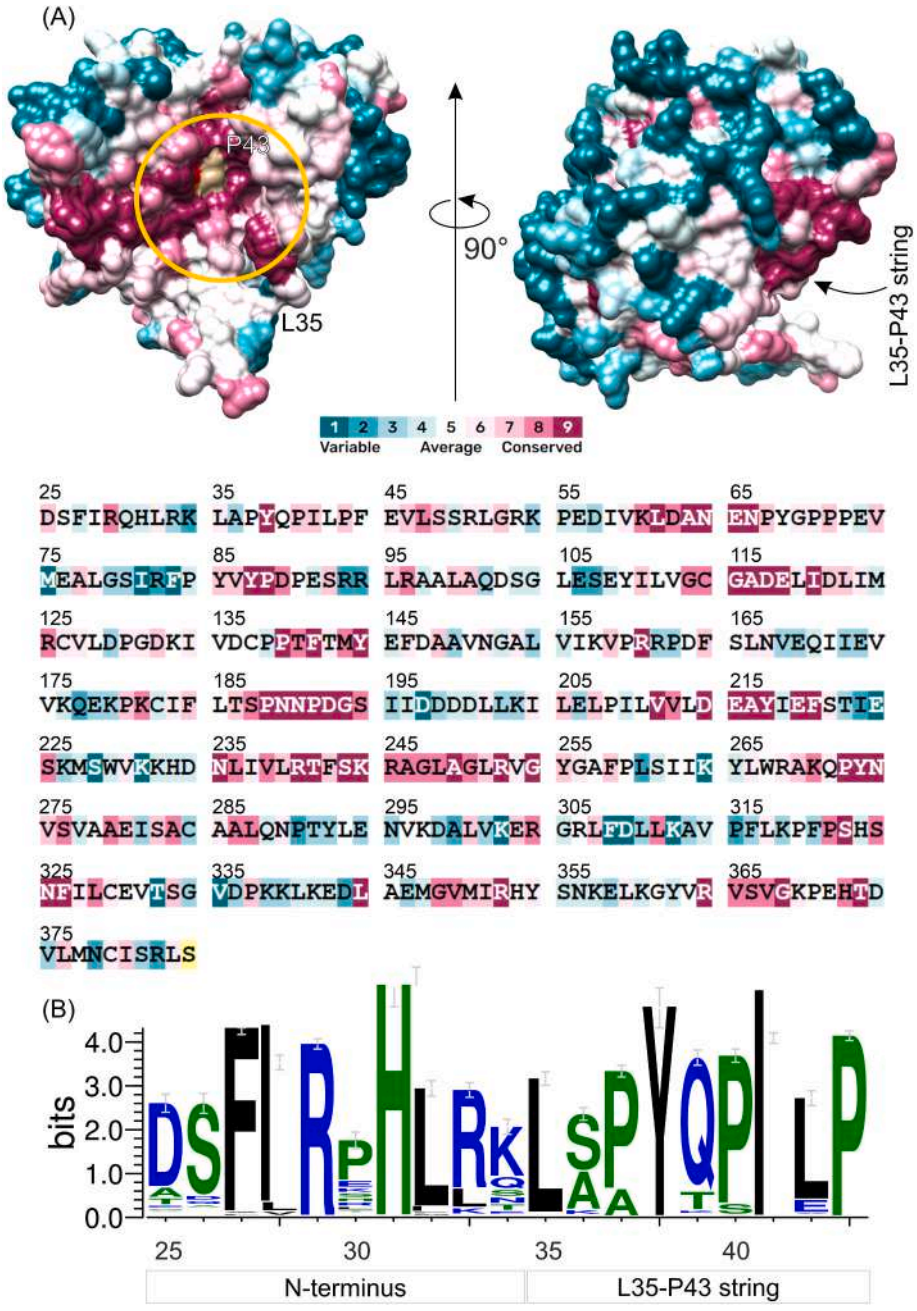

Fig. 6. Sequence conservation in *Mt*HISN6. The visual presentation of conservation scores (according to the color-key) obtained by analysis of 500 homologous sequences by *Consurf* is shown in (A). The active site region is marked by the yellow circle. The khaki surface region in the top-left panel marks the position of PLP; pale yellow highlight of S384 in the sequence indicates "insufficient data" for comparisons. Panel (B) shows sequence conservation in the N-terminus and the L35-P43 string among 349 HISN6 homologs in plants.

(Fig. 5B–D). The small domain (especially the fragment R352-K360) also moves towards the active site upon HOLP binding. We also observed adaptations in the residue conformations triggered by HOLP binding (Fig. 5C). Namely, the side chains of Y354 and R352 twist outward from the active site. This creates the environment for a firm locking of the negatively charged phosphate group of HOLP within the active site (Fig. 5B–D). Furthermore, the pyridine ring of PLP turns ~20° to attain a position almost parallel to the phenyl ring of F141.

Our apo*Mt*HISN6 structure allows us to infer rearrangements that accompany the binding of PLP. The electron density of the fragment K34–S48 (that contains the string region) is partial; the map does not cover most side chains, whereas I41 and L42 lack the density even for the backbone. The apo*Mt*HISN6 structure is most similar to the open form, as indicated by the reciprocal position between small and large domains and the residual electron density of the fragment K34–S48 corresponding with the open conformation of the string. This region becomes structured upon the PLP binding thanks to an extended net of water-mediated contacts.

2.5. Sequence conservation of HATs

We analyzed 500 sequences (261 of which contained the N-terminal part) that sampled 2247 homologous entries from the Uniref90 database using Consurf (Suzek et al., 2015; Ashkenazy et al., 2016) to gain more insights into residue conservation in HAT enzymes. The visual inspection of color-coded results mapped on the structure of HAT revealed that the core of the enzyme, the active site, and the dimerization interface are highly conserved (Fig. 6A). Interestingly, only Y38 (H-bonding the phosphate and imidazole of HOLP) is conserved among almost all analyzed sequences that contain the N-terminal part, with two exceptions where Phe substitutes it. Other solvent-exposed side chains vary among HATs of different origins.

Using 349 sequences of plant HISN6 homologs retrieved from the InterPro database, we analyzed the conservation of the L35-P43 string and the preceding N-terminal sequence (Fig. 6B). Interestingly, despite its flexible nature, the sequence of the L35-P43 string is conserved among plant homologs, except for A36, which is substituted by Ser or Lys. Moreover, the string in plants contains three Pro residues (P37, P40, and P43 in *Mt*HISN6) that make the string more rigid. While some variability is noted, the sequence of *Mt*HISN6 is dominant among plants. Also, the N-terminus in *Mt*HISN6 (residues 25–34) contains the highest-consensus sequence in plants except for a rarely occurring Q30 (Fig. 6B). Altogether, apparent differences between *Mt*HISN6 and bacterial homologs as well as high sequence conservation of HISN6 enzymes in plants make *Mt*HISN6 an excellent model for the research on the plant HBP.

2.6. Structural comparison with homologs of bacterial origin

Escherichia coli HAT (eHspAT) and *Mt*HISN6 share 31% sequence identity. The open states superpose with the RMSD 1.61 Å calculated for Cα atoms (PDB ID: 1gew (Haruyama et al., 2001)). However, due to the lack of convincing electron density, the string was not modeled in open eHspAT. The string was also absent in the electron density in the complex of eHspAT with PLP-Glu external aldimine (PDB ID: 1gey (Haruyama et al., 2001),). For this reason, we compared the closed states of

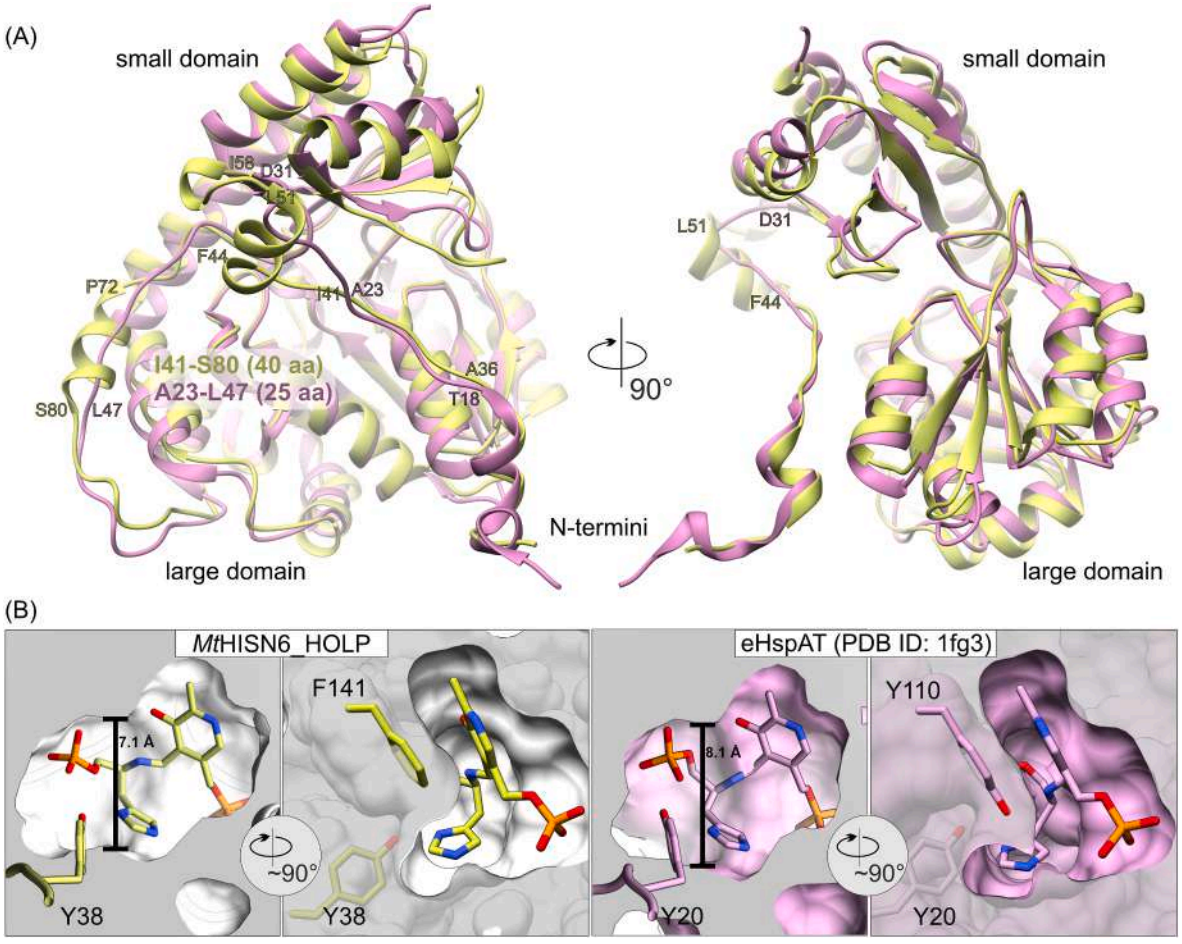

Fig. 7. Comparison of *Mt*HISN6 (green) with HAT from *E. coli* (eHspAT) (violet). Panel A shows the superposition of both structures with bound HOLP (PDB ID: 1fg3 for eHspAT). Cross-sections of the HOLP binding sites are presented in panel B; both surfaces were clipped at the same plane.

both enzymes in complexes with HOLP (RMSD 1.65 Å), using the structure by Sivaraman and coworkers (2001), who modeled the whole length of the chains starting from T3 (PDB ID: 1fg3). While the overall folds of *Mt*HISN6 and eHspAT are analogous, significant variations are evident in their secondary structure elements (Fig. 7A). The most striking differences occur in the small domains. The two enzymes differ significantly in how their N-terminal parts are affixed to the small domain. In *Mt*HISN6, the string is followed by an α-helix (F44-L51), a sharp turn, a β-strand (V59-L61), a linker, and an α-helix (P72–S80) that starts the large domain (Fig. 7A). The discussed range spans 40 residues in *Mt*HISN6 (I41–S80). The equivalent fragment in eHspAT is only 25 residues long (A23-L47) and contains a short loop (T18-D31) followed by a β-strand and a loop (W33-T38). Since the range encompasses the end of the string, its structure may play a role in maintaining the "tension" of the string so that its oscillation "stays in tune" with the reaction. In *Mt*HISN6, the fragment also fills in the indent between the subunits, thereby providing rigidity to the functional dimer. Comparing open (PDB IDs: 1fg7, 1iji) and closed (PDB IDs: 1fg3) states of available fully modeled eHspAT, the string region (L17-G27) in eHspAT adopts the same conformation with no hint of movement accompanying the change from the open to the closed state. The N-terminal fragment of the string (L17-S22) positions analogically to the *Mt*HISN6 string in the closed state, while A23-G27 point away from the active site entrance. Hence, in bacterial eHspAT the open/closed conformational change is based on the hinge-like movement of the small domain towards the active site rather than the movement of the string.

The sequence of the catalytic site is, unsurprisingly, one of the most conserved regions of HATs (Fig. 6A). The single difference we observe in *E. coli* is the presence of Y110 residue instead of F141 in *Mt*HISN6; these residues stack with the pyridine ring of PLP (Fig. 7B). The angle between the PLP and F/Y rings varies from 12° (PDB ID: 1gew) to 20° among different species and counts 17° for *Mt*HISN6. However, a comparison of the external aldimine complexes with HOLP shows that the HOLP binding site of *Mt*HISN6 is tighter (Fig. 7B). The narrow section of the active site measures 7.1 Å in *Mt*HISN6 compared to 8.1 Å in eHspAT. In effect, there is significantly less space near the HOLP imidazole moiety. It should be more difficult to accommodate an even bulkier phenyl of Phe to fit in the *Mt*HISN6 active site, which explains why *Mt*HISN6 did not transaminate Phe.

Since eHspAT lacks a biochemical description, we also compared *Mt*HISN6 to HAT from *Mycobacterium tuberculosis* (mHspAT) (Nasir et al., 2016). Superposition of the structures reveals higher RMSD values: (i) open onto open (PDB ID: 4rae, RMSD 2.7 Å, Fig. 8A) and (ii) closed onto closed (PDB 4r8d, 1.9 Å, Fig. 8B). In general, the differences between *Mt*HISN6 and mHspAT are similar to those noted in comparison with eHspAT. Moreover, in open mHspAT, the dimer mate slips into the active site of a subunit, displacing the whole N-terminal part, including the anchoring region (D25-R33). A long loop (S128-T137) within the large domain becomes an α-helix in the closed state. For *Mt*HISN6, the conformational changes are limited to the string open/closed transition

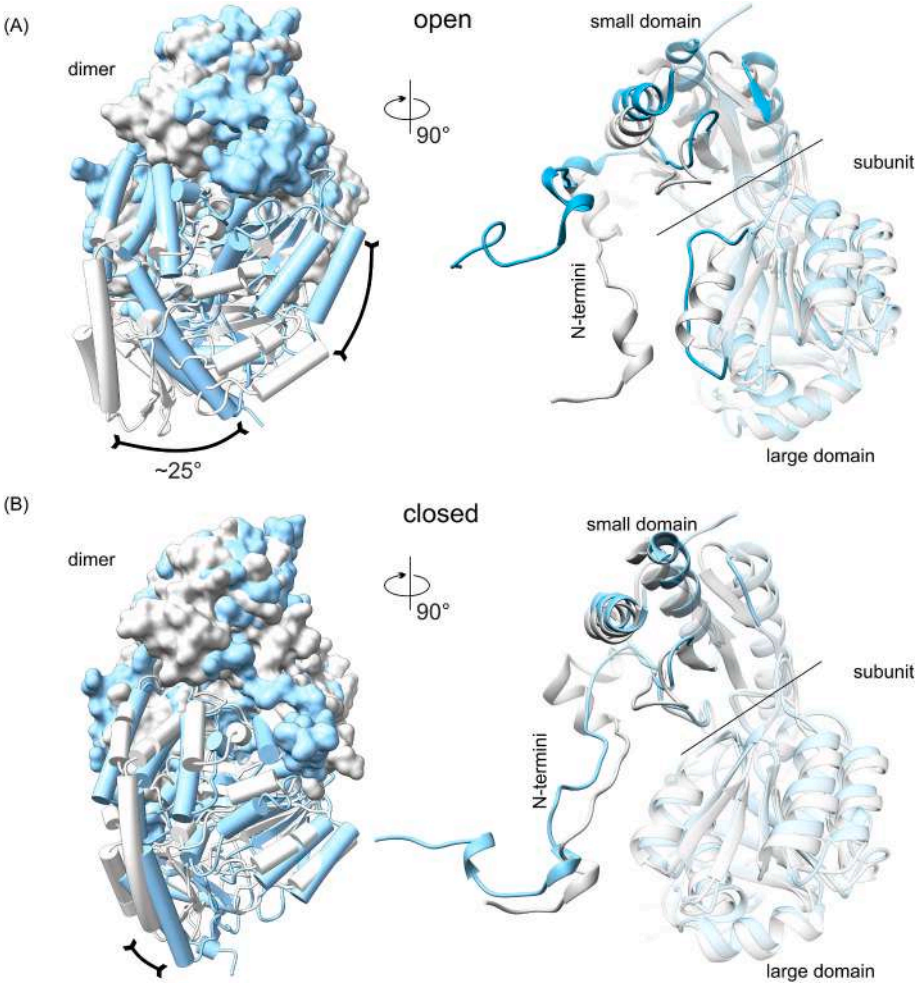

Fig. 8. Superposition of open (A) and close (B) structures of *Mt*HISN6 (white) and mHspAT (blue; PDB IDs: 4rae (A) and 4r8d (B)). The open-form structures differ significantly, especially in the small domain region, while the backbone of the closed forms superposes quite well, with most striking differences noticeable in the N-terminal regions. The approximate border between the small and large domains is marked by the black lines.

and a minor rotation of the small domain (Fig. 4B). This conformational flexibility provides a viable explanation why mHspAT has a significantly higher turnover rate (426 s^{-1}) but lower substrate affinity (K_M 420 μM). In the case of *Mt*HISN6, upon the substrate binding, the string moves further into the active site (by 3.7 Å), reducing its volume significantly. Notably, the high K_M values are a universal feature among studied bacterial homologs.

2.7. Dynamics of MtHISN6

To investigate the dynamics of *Mt*HISN6, we superposed our crystal structures in the open and closed states at their large domains (Fig. 4B; RMSD 0.79 Å). The rotational closing movement of the small domain displaces T291-F316, K348-D336, and K369–S384 helices and the linking fragments. Nonetheless, this movement is less pronounced than in mHspAT or eHspAT. As stated above, the most striking changes occur in the N-terminal part, including the P35-L43 string. The average displacement of the string is ~6.5 Å, reaching as far as 8.9 Å at P40 Cα. The following α-helical fragment, F44-D57, bends toward the active site, with an average displacement of 2 Å at Cα during structure closing. The open/close movement of the string is also accompanied by the side-chain movement of T265, R268, and a slight displacement of the main chain on the I263*-N274* and R352-R364 fragments. At the same time, the fragment D25-K34 stays anchored to the dimer mate's large domain, and the relative positions of two chains forming the dimer remain almost unaffected.

To evaluate the effect of HOLP binding on *Mt*HISN6, we performed 100-ns molecular dynamics (MD) simulations. The simulations were performed with two *Mt*HISN6 complexes with free K244, *i.e.*, complexes with PMP (modeled) and PLP-HOLP external aldimine to minimize bias and limit restrictions to the protein atoms. The results of MD simulations are consistent with the L35-P43 string participating in the active site formation upon the substrate binding (Fig. 9A and B). It is also clear that the binding of HOLP stabilizes the string, as the root-mean-square fluctuations (RMSFs) for Cα atoms decrease by half (Fig. 9C). On the other hand, we observe both open and close states in the absence of HOLP. Our crystal structures and the MD simulations are consistent with this regard. Uncoupling the dynamics of the *Mt*HISN6 string from ligand binding is a novelty. Such behavior may apply to other HATs, or at least be a universal feature of plant HISN6 enzymes, given the high sequence conservation of the string (Fig. 6B).

2.8. Virtual screening of soluble lead-like molecules

The HBP is absent in animals but is critical for plant growth. Thus, targeting plant HAT enzymes is a promising approach to the design of novel herbicides. The dynamics of *Mt*HISN6, especially the movement of the L35-P43 string, prompted us to exploit this region in the search for HISN6 inhibitors. Such molecules could lock the L35-P43 string in the open conformation, thus preventing it from closing, which is indispensable for providing proper reaction conditions.

We performed *in silico* docking of more than 1.35 mln soluble lead-like molecules downloaded from the ZINC database (Sterling and Irwin, 2015). The search box covered the area around the L35-P43 string of the *Mt*HISN6_open crystal structure. This way, we mapped druggable sites near the string while screening a vast chemical space. The chemical formulas and binding energies of the most potent 95 binders are provided in Supplementary Fig. S2.

The group of top hits are expected to bind in three distinct regions (Fig. 10A), with estimated binding energies up to −10.8 kcal/mol. They all have the potential to prevent the string from closing. Region 1 is located near the intersubunit interface between the small domains. ZINC9009723 (Fig. 10B) tightly fills the void between the outer ridge of the string and the small domain, while ZINC5013760 hints at the possibilities of linking Region 1 bound molecules with Region 2 bound molecules.

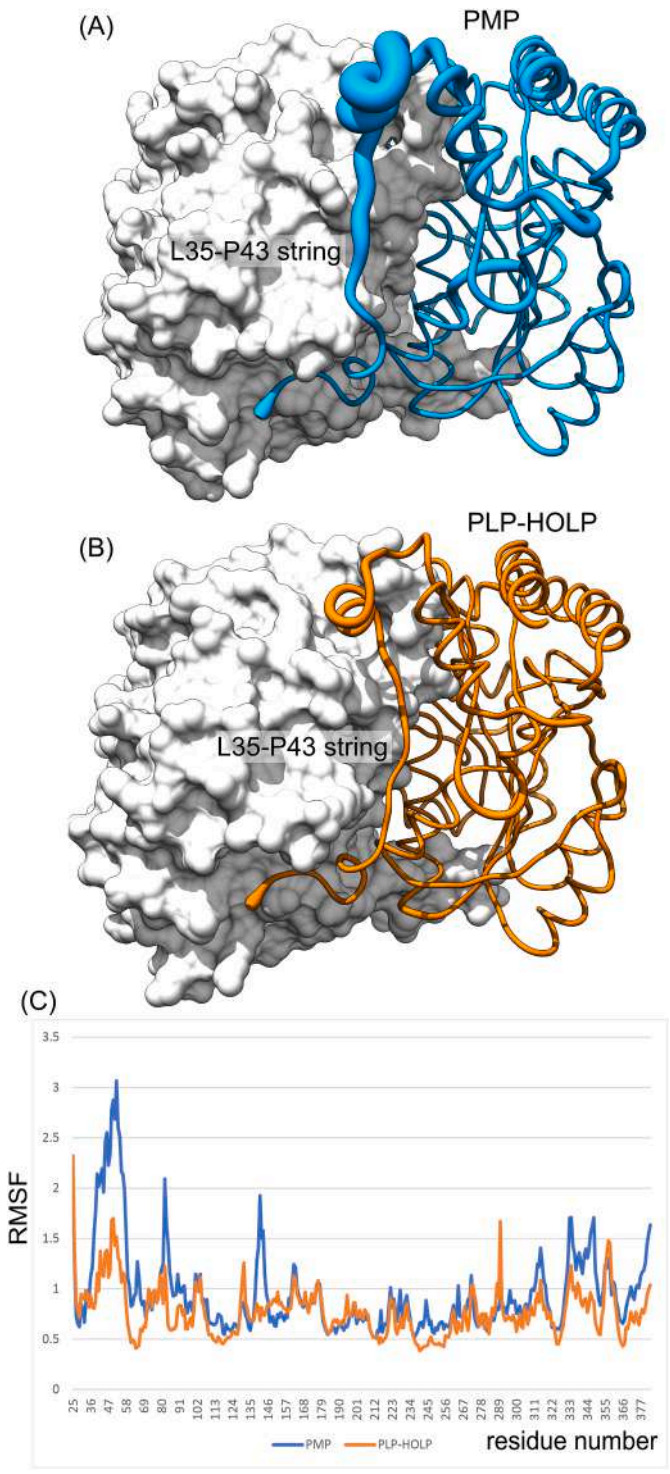

Fig. 9. Molecular dynamics simulations on *Mt*HISN6. Modeled complexes with PMP and PLP-HOLP (both external aldimines) are presented in panels A and B; one subunit is depicted as a white surface for clarity. The illustrations were created in UCSF Chimera (Pettersen et al., 2004) by presenting the B-factors calculated in Gromacs (Abraham et al., 2015) as widths of the "worms". The per residue root-mean-square-fluctuation (RMSF) of Cα atoms is shown in panel C.

Region 2 starts "behind" P43 and stretches towards the active site. The top-scoring molecules have a tetrazolopyridazine ring, locked in the site recognizing the phosphate group of HOLP, and interacting with R364 and PLP (ZINC95393759 (Fig. 10C), ZINC11085217, ZINC95350149). Interestingly, the substitution of the 1,2,4-triazole ring, situated in the middle of the molecule (ZINC95393759), by the

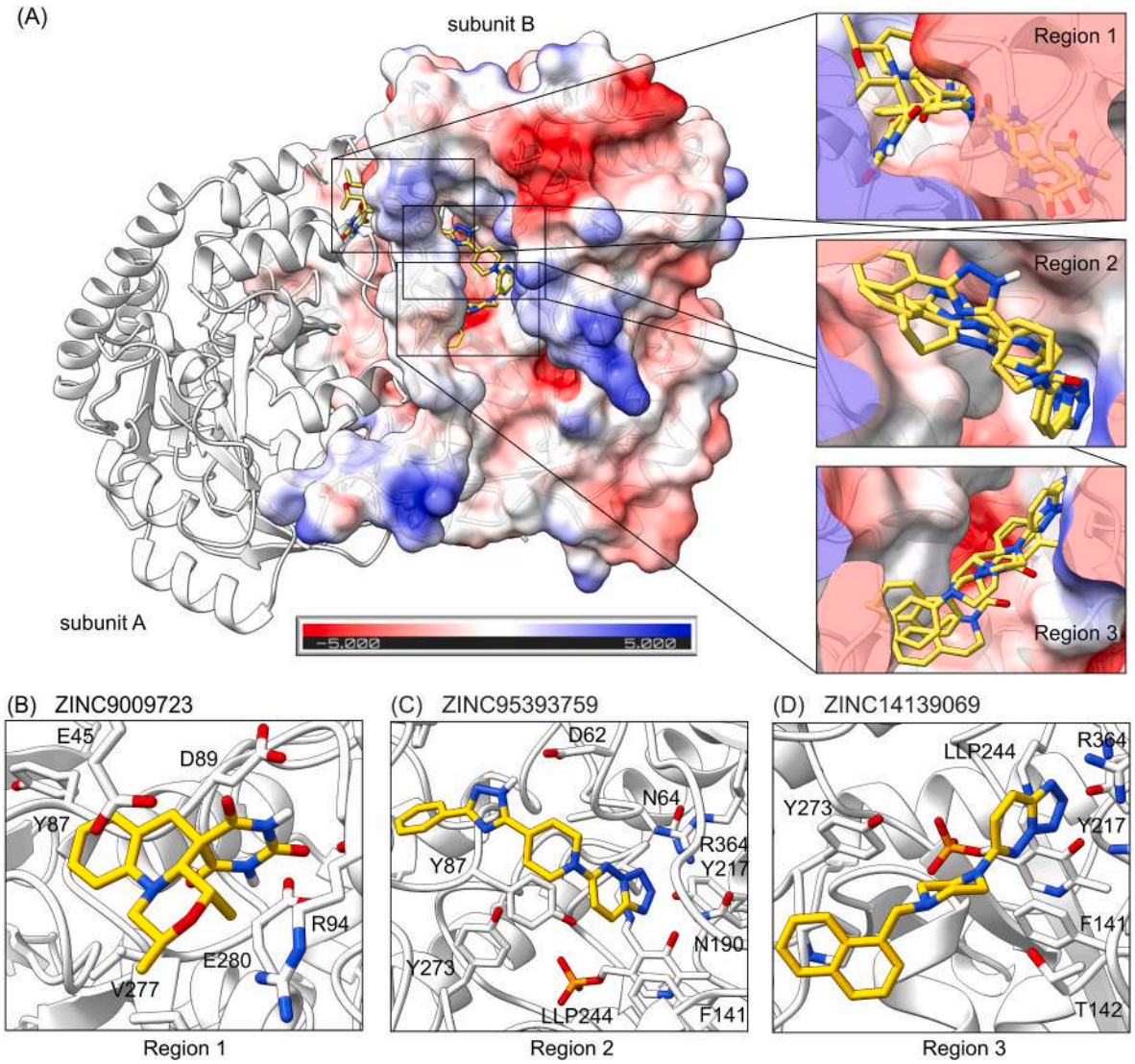

Fig. 10. The search region for the virtual screening campaign was oriented around the L35-P43 string. The molecules are predicted to bind in three slightly overlapping regions around the top part of the string. The three best scoring molecules in each region are presented as sticks with the *Mt*HISN6 surface electrostatic potential in the background (A). Detailed views over the three binding Regions (1–3) and their top-scoring binders are shown in panels B–D, respectively.

1,2,4-oxydiazole ring (ZINC95350149) decreases the estimated binding energy by 0.3 kcal/mol. The phenyl group on the other end of the molecule binds in a small tunnel between the top of the string and the small domain (ZINC95393759, ZINC12323188, ZINC95350149).

Region 3 starts at the heart of the active site, near PLP, and stretches along the large domain edge (T142-F146) towards A36 in the string. The top scoring molecules bind at the phosphate-binding site either using tetrazolopyridazine ring (ZINC14139069 (Fig. 10D)) or tetrazole group (ZINC65566055, ZINC33238693, ZINC5673503, ZINC72140159). The presence of negatively charged groups within the center of the binder has a beneficial effect on the binding energy (ZINC65566055 *vs*. ZINC5673503). Obtained results suggest that the best binders to Region 3 consist of the bicyclic aromatic moiety at the other end of the molecule (ZINC14139069, ZINC65566055, ZINC5673503, ZINC67674282).

3. Discussion

The evolution of plant HISN6 enzymes towards higher substrate selectivity is a phenomenon that was never described. Results obtained by SSN indicate that plant HISN6 evolved from a bacterial group, *Chloroflexota,* unlike many other chloroplast proteins that originate from *Cyanobacteria.* Interestingly, both *Chloroflexota* and *Cyanobacteria* are able to photosynthesize. However, most *Chloroflexota* conduct anoxygenic photosynthesis, a more primitive form than oxygenic photosynthesis (Shiha et al., 2017; West-Roberts et al., 2021). The origin of plant HISN6 enzymes from *Chloroflexota* is an unusual indication of plant evolution via horizontal gene transfer (HGT). A few other examples of HGT from bacteria to higher plants include genes essential for survival on the land (Yue et al., 2012, 2013). One such example is phenylalanine ammonia lyase (PAL) which was transferred from soil bacteria or fungi (Emiliani et al., 2009). PAL catalyzes the first step of the phenylpropanoid pathway that is responsible for the production of compounds such as flavonoids and lignin that are essential for the protection against UV light and the formation of xylem, respectively. Genes encoding for proteins associated with vascular tissue formation were also acquired from bacteria, e.g., the vein patterning 1 protein (VAP1) or TAL-type transaldolase (TAL) (Jun et al., 2002; Yang et al., 2015). In previous works, we found out that another HBP enzyme, *Mt*HISN2, is most similar to homologs from the class of *Deltaproteobacteria* (now referred to as *Myxococcota* (Oren and Garrity, 2021; Witek et al., 2021). Hence, there is increasing evidence that many genes associated with cellular metabolism and survival on land were likely obtained from bacteria and later

evolved in plants. There is a pending question about the driver of the HGT in the case of plant HISN6 enzymes. Perhaps HATs from *Cyanobacteria* were not selective enough to ensure optimal metabolism inside the chloroplasts? HGT from *Chloroflexota* might have given plants evolutionary benefits, thereby satisfying the selective pressure. According to the Brenda database (Chang et al., 2021), *Bacillus subtilis* HAT exhibits the lowest K_M with HOLP (150 μM) among the studied homologs (Weigent and Nester, 1976). This still is five-fold higher than K_M of *Mt*HISN6. Currently, no data for any other plant species or *Cyanobacteria* are available.

The N-terminal part of the small domain has previously been indicated as responsible for the substrate specificity of bacterial HATs; it is built by hydrophilic residues that allow the binding of HOLP (Nasir et al., 2012, 2016). The comparison between the open and closed forms (including the HOLP complex) reveals that the binding of HOLP induces conformational changes. Given the structural similarity, the binding of IAP, which is the substrate in the forward direction of the HBP, is most likely similar to that of HOLP. Analysis of the *Mt*HISN6_HOLP structure allowed us to determine the Y38, D117, N190, R352, and R364 as the critical residues in HOLP recognition.

For broad-specificity aminotransferases, a certain ambiguity occurs in substrate preference (Vernal et al., 1998, 2003; Matsui et al., 2000; Fernandez et al., 2004). In such cases, the active site adapts its volume to fit smaller and bulkier substrates by modifying the extent of the small domain movement and conformational change of the so-called arginine switch (Wen et al., 2015; Bujacz et al., 2021). In *Mt*HISN6, Y38 plays a similar role, firmly closing the active site and limiting its size. Furthermore, the three conserved Pro residues (P37, P40, and P43) likely brought about the structural integrity of the closed active site in plant HISN6 enzymes. The contribution of the N-terminal part of the small domain in the regulation of size and accessibility of the active site has been indicated in mHspAT. However, when we compare the substrate profile of the two HATs, mHspAT can process both HOLP and Phe, while *Mt*HISN6 is HOLP-selective. This is consistent with the higher rigidity of the *Mt*HISN6 string, which makes the enzyme unable to accommodate other substrates. Furthermore, the P35-L43 string of *Mt*HISN6 moves further into the active site upon the substrate binding than the homologous region of mHspAT.

Our data suggest that the low turnover rate is the cost that *Mt*HISN6 pays for high substrate affinity. However, the high substrate affinity allows efficacy at low substrate concentrations *in vivo*. Unfortunately, we were not able to measure the activity in the HBP forward direction (IAP → HOLP) because IAP is not available. It must also be remembered that the subsequent reaction in the HBP, *i.e.*, the dephosphorylation of HOLP into L-histidinol by HISN7, is irreversible and therefore shifts the equilibrium towards His production (Petersen et al., 2010; Ruszkowski and Dauter, 2016).

Some inhibitors of plant aminotransferases are available, but none of them is HISN6-selective. For instance, aminoethoxyvinylglycine can deregulate histidine homeostasis in plants (Le Deunff et al., 2019). However, not only does it impact other aminotransferases in plants, it affects other organisms as well. Hence, the closing of the string L35-P43 has caught our eye, as it is clearly indispensable for catalysis. Targeting the string region, which is highly conserved in plant HISN6 enzymes, would restrict the string rearrangement to build the active site and could be an efficient approach toward HISN6 inhibition. We performed a virtual screening to get the first glimpse of specific regions near the string and chemical moieties predestined for binding. The results mapped three hot spots in the string neighborhood and indicated the development direction for HISN6 inhibitors that could become herbicides. Using the top-scoring molecules within each region, one may envision a molecule with a linker between moieties docking to different regions. This could anchor the molecule in the interdomain area, entwine the string from behind, and occupy vast space at the entrance of the catalytic site – preventing its closing. Certain redundancy within the group of top binders may provide a starting point for establishing a structure-activity relationship (SAR).

Moreover, despite the high concentration of MES buffer (100 mM) in our crystallization trials, we do not observe MES molecules binding to *Mt*HISN6. This is in contrast to the case of mHspAT, where MES molecules bound in the active site and mimicked HOLP (Nasir et al., 2016). The sulfate ions present in our open-state structures could also serve as placeholders for negatively charged groups of new HISN6 inhibitors. Two sulfates bound in the active sites, while others occupy small clefts between the large and small domains, possibly locking the enzyme in the open state. Consistently, no sulfates are bound to the protein in our *Mt*HISN6_HOLP complex, which is the closest mimic of the *Mt*HISN6 active state.

4. Conclusions and outlook

As a result of the functional and structural study of *Mt*HISN6, here we provide a detailed insight into the evolution and characteristics of plant HISN6 enzymes. The calculated SSN suggests that plant HISN6 enzymes had been acquired by an HGT from *Chloroflexota* to have undergone further evolution within plants. The observed high substrate affinity and low turnover rate of *Mt*HISN6 can be attributed to the architecture of the active site that is tighter than that of bacterial counterparts with known structures. The closing of the highly-conserved in plants string region (residues L35-P43 in *Mt*HISN6) occurs dynamically – regardless of whether the substrate is bound in the active site or not. However, the substrate binding stabilizes the string in the closed state. On the other hand, the string must be closed to build a fully-functional active site. The high sequence conservation emphasizes the importance of the string for plant HISN6 activity, making the string dynamics a druggable site for HISN6-targeted herbicide development. Many plant species, unlike *A. thaliana*, possess a single HISN6 enzyme. Future research will show whether inhibition of HISN6 results in histidine starvation, accumulation of toxic levels of IAP, or impact signaling pathways linked to primary root growth (Mo et al., 2006). A phenotypic synergy may, in this case, enhance the efficacy of HISN6 inhibitors. Therefore, this work, which is a part of the project on deciphering the structures of the plant HBP enzymes, not only brings advancement in our understanding of the pathway at the molecular level but also provides the groundwork for the rationalized discovery of HISN6-targeted herbicides.

5. Materials and methods

5.1. Cloning, overexpression and purification of MtHISN6

The *Mt*HISN6 expression construct was produced using the protocol described for *Mt*HISN2 (Witek et al., 2021). In brief, total RNA isolated from *M. truncatula* leaves using the RNeasy Plant Mini Kit (Qiagen), was reverse-transcribed into the complementary DNA (cDNA) with SuperScript II reverse transcriptase (Life Technologies). The open reading frame coding for *Mt*HISN6 was amplified by polymerase chain reaction (PCR). The N-terminal signal peptide was excluded from the construct based on the prediction of the mature sequence based on TargetP 1.1 (Emanuelsson et al., 2000) prediction and by comparison of homologous sequences from other plant species. Based on this, the final construct was N-terminally truncated at D25 (UniProt ID: A0A072U7F9), whereas the C-terminus was not modified. The following primers were used for PCR: Forward, TACTTCCAATCCAATGCCGACTCCTTTATCAGACAACATCTC AGGA; Reverse: TTATCCACTTCCAATGTTACTACGATAGTCTGCTTA TGCAATTCATCA. The pMCSG68 vector (Midwest Center for Structural Genomics, USA) served to create the expression plasmids by the ligase-independent cloning method (Kim et al., 2011). The plasmids were used to transform *E. coli* BL21 (DE3) Gold competent cells for protein expression. The correctness of the coding sequence was verified by DNA sequencing.

Overexpression was conducted in BL21 Gold *E. coli* cells (Agilent Technologies). Lysogeny broth (LB) culture medium was supplemented

with 150 μg/mL ampicillin. The cultures were incubated at 37 °C and shaken at 180 RPM until A_{600} reached the value of 1.0. The cultures were cooled down to 18 °C and induced using isopropyl-D-thiogalactopyranoside (IPTG) at final concentration of 0.5 mM. The cultures were then shaken for another 18 h. After that time, the cultures were centrifuged at 4000×*g* for 15 min at 4 °C and resuspended in 30.0 mL of binding buffer [50 mM Hepes-NaOH, pH 7.5; NaCl 500 mM; imidazole 20 mM; 2 mM tris(2-carboxyethyl)phosphine (TCEP)]. The resuspended bacterial cell pellet was deep frozen at −80 °C and stored for purification.

The bacterial cell pellet was thawed and disrupted by sonication (5 min) with intervals for cooling. Cell debris was removed by centrifugation at 25,000×*g* for 30 min at 4 °C. The supernatant was mixed with 3 mL of HisTrap HP resin (GE Healthcare) and incubated for 3 min in a column on the VacMan pump (Promega). The resin with bound protein was thoroughly washed with 400 mL of binding buffer and eluted with 15 mL of elution buffer (50 mM Hepes–NaOH pH 7.5; 500 mM NaCl; 400 mM imidazole; 2 mM TCEP). In order to remove the His_6-tag, tobacco etch virus (TEV) protease was added at a final concentration of 0.2 mg/mL. Cleavage was conducted overnight at 4 °C, simultaneously with dialysis (SnakeSkin™ Dialysis Tubing, Thermo Fisher) to lower the imidazole concentration down to 20 mM. Except for the apo*Mt*HISN6, PLP at 10 μM concentration was added to the external dialysis solution. The sample was loaded again onto a column containing HisTrap HP resin, and *Mt*HISN6 was eluted from the column. The sample was concentrated to ca. 2.0 mL using Amicon Ultra 15 mL centrifugal filters (Merck) and loaded onto a HiLoad Superdex 200 16/60 column (GE Healthcare). The column was previously equilibrated with size exclusion buffer (25 mM Hepes–NaOH pH 7.5; 100 mM KCl; 50 mM NaCl; 1 mM TCEP). After elution, the protein was concentrated using Amicon Ultra 15 mL centrifugal filter.

5.2. Activity assays

The aminotransferase activity of *Mt*HISN6 was measured using a coupled assay with bovine GDH. HOLP (lithium salt, Merck 41,486) was used to measure the activity in the reverse reaction (with respect to the HBP) as IAP is not commercially available. Concentrations and amounts of the constant components of the reaction mixtures were established in our preliminary experiments to be as follows: (i) forty units of bovine GDH (sigma G2626, sufficient to prevent the coupled reaction from being rate-limiting); (ii) *Mt*HISN6, 2 μM; (iii) NAD^+, 1 mM; (iv) 2OG, 2 mM; (v) PLP, 2 μM and (vi) HOLP (or Phe) at varied concentrations. We also tested *A. thaliana* GDH1 (Grzechowiak et al., 2020), but this isoform was not applicable due to the high K_M. The reaction buffer was 25 mM HEPES-NaOH pH 7.5, 100 mM KCl, 50 mM NaCl. Measurements were performed on a Hewlett-Packard 8453 diode-array spectrophotometer (Agilent Technologies, Santa Clara, CA) in 800 μL volumes in duplicate. The formation of NADH was monitored continuously (2 Hz) through absorbance at 340 nm wavelength. Data were fit to the Michaelis-Menten equation using the GraphPad Prism 6.07 software. No detectable activity was present for Phe up to 25 mM concentration.

The binding of HOLP and Phe was compared by measuring the formation of the external aldimine, monitored by absorbance increase at around 355 nm for 4 min. The assay was performed in the mixture containing 25 mM HEPES-NaOH pH 7.5, 100 mM KCl, 50 mM NaCl, 20 μM PLP, and 20 μM *Mt*HISN6. Either Phe or HOLP was added at 1 mM final concentration. Results were analyzed in Spectragryph 1.2 (Spectroscopy Ninja).

5.3. Crystallization and diffraction data collection

MtHISN6 was crystallized using the vapor diffusion method in a sitting drop setup. The protein was concentrated to 18.8 mg/mL. The concentration was determined spectrophotometrically at A_{280} using the molar extinction coefficient of 30,870. *Mt*HISN6_open form crystals grew in 90% of the C10 solution from the BCS screen (Molecular Dimensions), *i.e.*, 0.18 M ammonium sulfate, 0.09 M sodium acetate pH 4.6, 22.5% v/v PEG Smear Broad. The MtHISN6_closed form crystals were obtained from Index Screen G6 conditions (Hampton, USA): 0.2 M ammonium acetate; 0.1 M BIS-TRIS pH 5.5; 25% w/v polyethylene glycol 3350. The protein sample was supplemented with 1 mM PLP. As a cryoprotection, the mixture of the crystallization conditions with 20% ethylene glycol was used for both aforementioned forms. The latter crystals were used for soaking to obtain the *Mt*HISN6-HOLP complex. The cryoprotecting solution was supplemented with 0.2 μL of 200 mM HOLP added to 2 μL cryo drop. After a 10 min incubation, the soaked crystals were flash frozen. The apo*Mt*HISN6 crystals were obtained when no PLP was added to the protein sample before crystallization using the ShotGun (SG-1, Molecular Dimensions) in the B4 condition that contained the following components: 0.2 M ammonium sulfate; 0.1 M MES pH 6.5; 30% w/v PEG 5000 MME. The crystals were cryoprotected using SG-1 condition supplemented with 20% ethylene glycol. The crystals were vitrified in liquid nitrogen and stored for synchrotron data measurements.

Data were collected at the 22-ID beamline at the Advanced Photon Source, Argonne, USA or at the P13 beamline, PETRA, Hamburg, Germany. The diffraction images were processed *XDS* (Kabsch, 2010). The statistics of the data collection and processing are summarized in Table 1.

5.4. Determination and refinement of the crystal structures

The structure of *Mt*HISN6_open was solved by molecular replacement in *Phaser* (McCoy et al., 2007), using coordinates of *Cupriavidus pinatubonensis* JMP134 HAT (PDB ID: 3euc, unpublished) as a model; the sequences share 34% identity. The initial model of *Mt*HISN6 was obtained by sequence fitting in *Phenix.AutoBuild* (Afonine et al., 2012). The *Mt*HISN6_closed, *Mt*HISN6_HOLP and apo*Mt*HISN6_structures were solved by molecular replacement using *Mt*HISN6_open as a model. All four structures were refined by iterative cycles of manual rebuilding using *Coot* (Emsley P et al., 2010) and automated refinement in *Phenix.refine* (Liebschner et al., 2019). The geometric parameters and model-map correlation were validated in *MolProbity* (Williams et al., 2018) and the validation server of the PDB (Berman et al., 2000). The refinement statistics are listed in Table 1.

5.5. Virtual screening

A subset containing molecules of molecular weight 300–350 Da and logP ≤2 was derived from the lead-like library; 1,355,624 docking-ready files were downloaded from the ZINC15 database (Sterling and Irwin, 2015) in March 2022. Docking was performed in *AutoDock Vina* (Trott and Olson, 2010) using custom-made Python scripts, with the exhaustiveness = 8. *Mt*HISN6_open was prepared as the receptor for docking with the UCSF *Chimera* DockPrep tool (Pettersen et al., 2004). The search box with the dimensions of 33.9 × 28.0 × 33.3 Å was centered at 78.3, 30.7, 13.65 (x, y, z). The results were scored based on the calculated binding energy.

5.6. Molecular dynamics simulations

MD simulations were performed in *Gromacs 2021.5* (Abraham et al., 2015) with the AMBER99SB-ILDN force field applied (Lindorff-Larsen et al., 2010). *Mt*HISN6 complexes (created in *Coot* (Emsley P et al., 2010)) with either PMP or PLP-HOLP external aldimine were subjected to MD simulations independently to minimize bias. The model was solvated using TIP3P water model in a cubic box. Sodium cations were used to neutralize the system. Energy minimization was followed by NVT and NPT equilibrations, each for 50,000 of 2 fs steps. The production MD was run for a total of 100 ns (50,000,000 of 2-fs steps) at 300 K. The dynamics of the protein were evaluated based on

root-mean-square-fluctuation (RMSF) for Cα atoms, converted to B-factors using *Gromacs* internal tools and presented in UCSF *Chimera* (Pettersen et al., 2004) as worms.

5.7. Other software used

Molecular illustrations were created with UCSF *Chimera X* (Pettersen et al., 2021) and UCSF *Chimera* (Pettersen et al., 2004). RMSD values for the whole PDB search were taken from PDB-Fold (Krissinel and Henrick, 2004). A set of 500 sequences that samples 2247 unique homologs from UniProt (The UniProt, 2017) between 35 and 95% sequence identity to *Mt*HISN6 was created using Multiple Sequence Alignment using MAFFT and HMMER algorithm with an E-value of 0.0001. The conservation was analyzed with *ConSurf* (Ashkenazy et al., 2016). The 349 plant enzyme sequences were retrieved from InterPro database (Blum et al., 2021). Their MSA was prepared using the *Clustal Omega* webserver (https://www.ebi.ac.uk/Tools/msa/clustalo/) (Sievers et al., 2011). The distribution matrix was prepared using *WebLogo3* application (Crooks et al., 2004). The distribution of the surface electrostatic potential was calculated using *PDB2PQR* and *APBS* servers (Baker et al., 2001; Dolinsky et al., 2004). SSN analysis was calculated using the EFI-EST webserver (Zallot et al., 2019) from 21,142 UniRef90 (Suzek et al., 2015) sequences retrieved from the InterPro (Blum et al., 2021) family of L-histidinol phosphate aminotransferases (IPR005861). The alignment score was set to 100, while the sequence lengths were restricted to 320–440 residues. The graph was created in *Cytoscape 3.3* (Shannon et al., 2003).

Author contributions

M. Rutkiewicz refined the structures, analyzed them, and wrote the manuscript. IN performed the kinetic measurements with the help of SA; the data were analyzed by IN and RC. WW obtained the apoMtHISN6 structure and analyzed the HISN6 evolution. M. Ruszkowski obtained the other structures, wrote parts of the manuscript, and edited the text.

Declaration of competing interest

The authors declare that they have no known competing financial interests or personal relationships that could have appeared to influence the work reported in this paper.

Data availability

PDB IDs: crystal structure of *Medicago truncatula* histidinol-phosphate aminotransferase (HISN6) in the open state, 8bj1; crystal structure of *Medicago truncatula* histidinol-phosphate aminotransferase (HISN6) in the closed state, 8bj2; crystal structure of *Medicago truncatula* histidinol-phosphate aminotransferase (HISN6) in complex with histidinol-phosphate, 8bj3; crystal structure of *Medicago truncatula* histidinol-phosphate aminotransferase (HISN6) in apo form, 8bj4. Raw diffraction datasets are available from the MX-RDR (https://mxrdr.icm.edu.pl/) under the following DOIs (respectively): https://doi.org/10.18150/VHEKMI; https://doi.org/10.18150/BTMRJV; https://doi.org/10.18150/ZMHOTT; https://doi.org/10.18150/ZEPS7J. All other data, including the results of the virtual screening, will be shared upon request.

Acknowledgments

This project was supported by the National Science Centre grant number: SONATA 2018/31/D/NZ1/03630 to M. Ruszkowski and the Intramural Research Program of the NCI Center for Cancer Research. The synchrotron data were collected at the P13 beamline operated by EMBL Hamburg at the PETRA III storage ring (DESY, Hamburg, Germany (Cianci et al., 2017)) and at the SER-CAT beamline 22-ID at the Advanced Photon Source, Argonne National Laboratory, supported by the U.S. Department of Energy, Office of Science, Office of Basic Energy Sciences under Contract W-31-109-Eng-38.

Appendix A. Supplementary data

Supplementary data to this article can be found online at https://doi.org/10.1016/j.plaphy.2023.02.017.

References

Abraham, M., Murtola, T., Schulz, R., Páll, S., Smith, J., Hess, B., Lindahl, E., 2015. GROMACS: high performance molecular simulations through multi-level parallelism from laptops to supercomputers. Software 1, 19–25. https://doi.org/10.1016/j.softx.2015.06.001.

Afonine, P.V., Grosse-Kunstleve, R.W., Echols, N., Headd, J.J., Moriarty, N.W., Mustyakimov, M., Terwilliger, T.C., Urzhumtsev, A., Zwart, P.H., Adams, P.D., 2012. Towards automated crystallographic structure refinement with phenix.refine. Acta Crystallogr. D 68, 352–367. https://doi.org/10.1107/S0907444912001308.

Ashkenazy, H., Abadi, S., Martz, E., Chay, O., Mayrose, I., Pupko, T., Ben-Tal, N., 2016. ConSurf 2016: an improved methodology to estimate and visualize evolutionary conservation in macromolecules. Nucleic Acids Res. 44, W344–W350. https://doi.org/10.1093/nar/gkw408.

Baker, N.A., Sept, D., Joseph, S., Holst, M.J., Mccammon, J.A., 2001. Electrostatics of nanosystems: application to microtubules and the ribosome. Proc. Natl. Acad. Sci. U. S. A. 98, 10037–10041. https://doi.org/10.1073/pnas.181342398.

Beckie, H.J., Busi, R., Lopez-Ruiz, F.J., Umina, P.A., 2021. Herbicide resistance management strategies: how do they compare with those for insecticides, fungicides and antibiotics? Pest Manag. Sci. 77, 3049–3056. https://doi.org/10.1002/ps.6395.

Berman, H.M., Westbrook, J., Feng, Z., Gilliland, G., Bhat, T.N., Weissig, H., Shindyalov, I.N., Bourne, P.E., 2000. The protein Data Bank. Nucleic Acids Res. 28, 235–242. https://doi.org/10.1093/nar/28.1.235.

Blum, M., Chang, H.Y., Chuguransky, S., Grego, T., Kandasaamy, S., Mitchell, A., Nuka, G., Paysan-Lafosse, T., Qureshi, M., Raj, S., Richardson, L., Salazar, G.A., Williams, L., Bork, P., Bridge, A., Gough, J., Haft, D.H., Letunic, I., Marchler-Bauer, A., Mi, H.Y., Natale, D.A., Necci, M., Orengo, C.A., Pandurangan, A.P., Rivoire, C., Sigrist, C.J.A., Sillitoe, I., Thanki, N., Thomas, P.D., Tosatto, S.C.E., Wu, C.H., Bateman, A., Finn, R.D., 2021. The InterPro protein families and domains database: 20 years on. Nucleic Acids Res. 49, D344–D354. https://doi.org/10.1093/nar/gkaa977.

Bujacz, A., Rum, J., Rutkiewicz, M., Pietrzyk-Brzezinska, A.J., Bujacz, G., 2021. Structural evidence of active site adaptability towards different sized substrates of aromatic amino acid aminotransferase from psychrobacter. Sp. B6. Materials (Basel) 14. https://doi.org/10.3390/ma14123351.

Chang, A., Jeske, L., Ulbrich, S., Hofmann, J., Koblitz, J., Schomburg, I., Neumann-Schaal, M., Jahn, D., Schomburg, D., 2021. BRENDA, the ELIXIR core data resource in 2021: new developments and updates. Nucleic Acids Res. 49, D498–D508. https://doi.org/10.1093/nar/gkaa1025.

Cianci, M., Bourenkov, G., Pompidor, G., Karpics, I., Kallio, J., Bento, I., Roessle, M., Cipriani, F., Fiedler, S., Schneider, T.R., 2017. P13, the EMBL macromolecular crystallography beamline at the low-emittance PETRA III ring for high- and low-energy phasing with variable beam focusing. J. Synchrotron Radiat. 24, 323–332. https://doi.org/10.1107/S1600577516016465.

Crooks, G.E., Hon, G., Chandonia, J.M., Brenner, S.E., 2004. WebLogo: a sequence logo generator. Genome Res. 14, 1188–1190. https://doi.org/10.1101/gr.849004.

Dolinsky, T.J., Nielsen, J.E., Mccammon, J.A., Baker, N.A., 2004. PDB2PQR: an automated pipeline for the setup of Poisson-Boltzmann electrostatics calculations. Nucleic Acids Res. 32, W665–W667. https://doi.org/10.1093/nar/gkh381.

Duke, S.O., 2018. The history and current status of glyphosate. Pest Manag. Sci. 74, 1027–1034. https://doi.org/10.1002/ps.4652.

Emanuelsson, O., Nielsen, H., Brunak, S., Von Heijne, G., 2000. Predicting subcellular localization of proteins based on their N-terminal amino acid sequence. J. Mol. Biol. 300, 1005–1016. https://doi.org/10.1006/jmbi.2000.3903.

Emiliani, G., Fondi, M., Fani, R., Gribaldo, S., 2009. A horizontal gene transfer at the origin of phenylpropanoid metabolism: a key adaptation of plants to land. Biol. Direct 4, 7. https://doi.org/10.1186/1745-6150-4-7.

Emsley, P., Lohkamp, B., Scott, W.G., K, C., 2010. Features and development of Coot. Acta Crystallogr. D D66, 486–501. https://doi.org/10.1107/S0907444910007493.

Farina, W.M., Balbuena, M.S., Herbert, L.T., Gonalons, C.M., Vazquez, D.E., 2019. Effects of the herbicide glyphosate on honey bee sensory and cognitive abilities: individual impairments with implications for the hive. Insects 10, 354. https://doi.org/10.3390/insects10100354.

Fernandez, F.J., Vega, M.C., Lehmann, F., Sandmeier, E., Gehring, H., Christen, P., Wilmanns, M., 2004. Structural studies of the catalytic reaction pathway of a hyperthermophilic histidinol-phosphate aminotransferase. J. Biol. Chem. 279, 21478–21488. https://doi.org/10.1074/jbc.M400291200.

Ford, G.C., Eichele, G., Jansonius, J.N., 1980. Three-dimensional structure of a pyridoxal-phosphate-dependent enzyme, mitochondrial aspartate aminotransferase. Proc. Natl. Acad. Sci. USA 77, 2559–2563. https://doi.org/10.1073/pnas.77.5.2559.

Forlani, G., Mangiagalli, A., Nielsen, E., Suardi, C.M., 1999. Degradation of the phosphonate herbicide glyphosate in soil: evidence for a possible involvement of unculturable microorganisms. Soil Biol. Biochem. 31, 991–997. https://doi.org/10.1016/S0038-0717(99)00010-3.

Gaines, T.A., Busi, R., Kupper, A., 2021. Can new herbicide discovery allow weed management to outpace resistance evolution? Pest Manag. Sci. 77, 3036–3041. https://doi.org/10.1002/ps.6457.
Glynn, S.E., Baker, P.J., Sedelnikova, S.E., Davies, C.L., Eadsforth, T.C., Levy, C.W., Rodgers, H.F., Blackburn, G.M., Hawkes, T.R., Viner, R., Rice, D.W., 2005. Structure and mechanism of imidazoleglycerol-phosphate dehydratase. Structure 13, 1809–1817. https://doi.org/10.1016/j.str.2005.08.012.
Gould, F., Brown, Z.S., Kuzma, J., 2018. Wicked evolution: can we address the sociobiological dilemma of pesticide resistance? Science 360, 728–732. https://doi.org/10.1126/science.aar3780.
Grzechowiak, M., Sliwiak, J., Jaskolski, M., Ruszkowski, M., 2020. Structural studies of glutamate dehydrogenase (isoform 1) from Arabidopsis thaliana, an important enzyme at the branch-point between carbon and nitrogen metabolism. Front. Plant Sci. 11, 754. https://doi.org/10.3389/fpls.2020.00754.
Guyton, K.Z., Loomis, D., Grosse, Y., El Ghissassi, F., Benbrahim-Tallaa, L., Guha, N., Scoccianti, C., Mattock, H., Straif, K., Working, I.a.R.C.M., 2015. Carcinogenicity of tetrachlorvinphos, parathion, malathion, diazinon, and glyphosate. Lancet Oncol. 16, 490–491. https://doi.org/10.1016/S1470-2045(15)70134-8.
Haruyama, K., Nakai, T., Miyahara, I., Hirotsu, K., Mizuguchi, H., Hayashi, H., Kagamiyama, H., 2001. Structures of Escherichia coli histidinol-phosphate aminotransferase and its complexes with histidinol-phosphate and N-(5′-Phosphopyridoxyl)-L-Glutamate: double substrate recognition of the enzyme. Biochemistry 40, 4633–4644. https://doi.org/10.1021/bi002769u.
Jensen, R.A., Gu, W., 1996. Evolutionary recruitment of biochemically specialized subdivisions of family I within the protein superfamily of aminotransferases. J. Bacteriol. 178, 2161–2171. https://doi.org/10.1128/jb.178.8.2161-2171.1996.
Jun, J.H., Ha, C.M., Nam, H.G., 2002. Involvement of the VEP1 gene in vascular strand development in Arabidopsis thaliana. Plant Cell Physiol. 43, 323–330. https://doi.org/10.1093/pcp/pcf042.
Kabsch, W., 2010. Xds. Acta Cryst. D 66, 125–132. https://doi.org/10.1107/S0907444909047337.
Kim, Y., Babnigg, G., Jedrzejczak, R., Eschenfeldt, W.H., Li, H., Maltseva, N., Hatzos-Skintges, C., Gu, M.Y., Makowska-Grzyska, M., Wu, R.Y., An, H., Chhor, G., Joachimiak, A., 2011. High-throughput protein purification and quality assessment for crystallization. Methods 55, 12–28. https://doi.org/10.1016/j.ymeth.2011.07.010.
Krissinel, E., Henrick, K., 2004. Secondary-structure matching (SSM), a new tool for fast protein structure alignment in three dimensions. Acta Crystallogr. D 60, 2256–2268. https://doi.org/10.1107/S0907444904026460.
Le Deunff, E., Beauclair, P., Deleu, C., Lecourt, J., 2019. Inhibition of aminotransferases by aminoethoxyvinylglycine triggers a nitrogen limitation condition and deregulation of histidine homeostasis that impact root and shoot development and nitrate uptake. Front. Plant Sci. 10, 1387. https://doi.org/10.3389/fpls.2019.01387.
Liebschner, D., Afonine, P.V., Baker, M.L., Bunkoczi, G., Chen, V.B., Croll, T.I., Hintze, B., Hung, L.-W., Jain, S., Mccoy, A.J., Moriarty, N.W., Oeffner, R.D., Poon, B.K., Prisant, M.G., Read, R.J., Richardson, J.S., Richardson, D.C., Sammito, M.D., Sobolev, O.V., Stockwell, D.H., Terwilliger, T.C., Urzhumtsev, A.G., Videau, L.L., Williams, C.J., Adams, P.D., 2019. Macromolecular structure determination using X-rays, neutrons and electrons: recent developments in Phenix. Acta Crystallogr. D 75, 861–877. https://doi.org/10.1107/S2059798319011471.
Lindorff-Larsen, K., Piana, S., Palmo, K., Maragakis, P., Klepeis, J.L., Dror, R.O., Shaw, D. E., 2010. Improved side-chain torsion potentials for the Amber ff99SB protein force field. Proteins 78, 1950–1958. https://doi.org/10.1002/prot.22711.
Maeda, H., Dudareva, N., 2012. The shikimate pathway and aromatic amino acid biosynthesis in plants. Annu. Rev. Plant Biol. 63 (63), 73–105. https://doi.org/10.1146/annurev-arplant-042811-105439.
Matsui, I., Matsui, E., Sakai, Y., Kikuchi, H., Kawarabayasi, Y., Ura, H., Kawaguchi, S.-I., Kuramitsu, S., Harata, K., 2000. The molecular structure of hyperthermostable aromatic aminotransferase with novel substrate specificity from Pyrococcus horikoshii</em&gt. J. Biol. Chem. 275, 4871–4879. https://doi.org/10.1074/jbc.275.7.4871.
Mccoy, A.J., Grosse-Kunstleve, R.W., Adams, P.D., Winn, M.D., Storoni, L.C., Read, R.J., 2007. Phaser crystallographic software. J. Appl. Crystallogr. 40, 658–674. https://doi.org/10.1107/S0021889807021206.
Mo, X.R., Zhu, Q.Y., Li, X., Li, J., Zeng, Q.N., Rong, H.L., Zhang, H.M., Wu, P., 2006. The hpa1 mutant of Arabidopsis reveals a crucial role of histidine homeostasis in root meristem maintenance. Plant Physiol. 141, 1425–1435. https://doi.org/10.1104/pp.106.084178.
Motta, E.V.S., Raymann, K., Moran, N.A., 2018. Glyphosate perturbs the gut microbiota of honey bees. Proc. Natl. Acad. Sci. USA 115, 10305–10310. https://doi.org/10.1073/pnas.1803880115.
Muralla, R., Sweeney, C., Stepansky, A., Leustek, T., Meinke, D., 2007. Genetic dissection of histidine biosynthesis in Arabidopsis. Plant Physiol. 144, 890–903. https://doi.org/10.1104/pp.107.096511.
Nasir, N., Anant, A., Vyas, R., Biswal, B.K., 2016. Crystal structures of Mycobacterium tuberculosis HspAT and ArAT reveal structural basis of their distinct substrate specificities. Sci. Rep. 6, 18880 https://doi.org/10.1038/srep18880.
Nasir, N., Vyas, R., Chugh, C., Ahangar, M.S., Biswal, B.K., 2012. Molecular cloning, overexpression, purification, crystallization and preliminary X-ray diffraction studies of histidinol phosphate aminotransferase (HisC2) from Mycobacterium tuberculosis. Acta Crystallogr. F 68, 32–36. https://doi.org/10.1107/S1744309111045386.
Oren, A., Garrity, G.M., 2021. Valid publication of the names of forty-two phyla of prokaryotes. Int. J. Syst. Evol. Microbiol. 71 https://doi.org/10.1099/ijsem.0.005056.
Petersen, L.N., Marineo, S., Mandala, S., Davids, F., Sewell, B.T., Ingle, R.A., 2010. The missing link in plant histidine biosynthesis: Arabidopsis myoinositol monophosphatase-like2 encodes a functional histidinol-phosphate phosphatase. Plant Physiol. 152, 1186–1196. https://doi.org/10.1104/pp.109.150805.
Pettersen, E.F., Goddard, T.D., Huang, C.C., Couch, G.S., Greenblatt, D.M., Meng, E.C., Ferrin, T.E., 2004. UCSF Chimera-a visualization system for exploratory research and analysis. J. Comput. Chem. 25, 1605–1612. https://doi.org/10.1002/jcc.20084.
Pettersen, E.F., Goddard, T.D., Huang, C.C., Meng, E.C., Couch, G.S., Croll, T.I., Morris, J. H., Ferrin, T.E., 2021. UCSF ChimeraX: structure visualization for researchers, educators, and developers. Protein Sci. 30, 70–82. https://doi.org/10.1002/pro.3943.
Raven, J.A., Allen, J.F., 2003. Genomics and chloroplast evolution: what did cyanobacteria do for plants? Genome Biol. 4, 209. https://doi.org/10.1186/gb-2003-4-3-209.
Ruszkowski, M., 2018. Guarding the gateway to histidine biosynthesis in plants: Medicago truncatula ATP-phosphoribosyltransferase in relaxed and tense states. Biochem. J. 475, 2681–2697. https://doi.org/10.1042/BCJ20180289.
Ruszkowski, M., Dauter, Z., 2016. Structural studies of Medicago truncatula histidinol phosphate phosphatase from inositol monophosphatase superfamily reveal details of penultimate step of histidine biosynthesis in plants. J. Biol. Chem. 291, 9960–9973. https://doi.org/10.1074/jbc.M115.708727.
Ruszkowski, M., Dauter, Z., 2017. Structures of Medicago truncatula L-histidinol dehydrogenase show rearrangements required for NAD(+) binding and the cofactor positioned to accept a hydride. Sci. Rep. 7, 10476 https://doi.org/10.1038/s41598-017-10859-0.
Shannon, P., Markiel, A., Ozier, O., Baliga, N.S., Wang, J.T., Ramage, D., Amin, N., Schwikowski, B., Ideker, T., 2003. Cytoscape: a software environment for integrated models of biomolecular interaction networks. Genome Res. 13, 2498–2504. https://doi.org/10.1101/gr.1239303.
Shiha, P.M., Ward, L.M., Fischer, W.W., 2017. Evolution of the 3-hydroxypropionate bicycle and recent transfer of anoxygenic photosynthesis into the Chloroflexi. Proc. Natl. Acad. Sci. USA 114, 10749–10754. https://doi.org/10.1073/pnas.1710798114.
Sievers, F., Wilm, A., Dineen, D., Gibson, T.J., Karplus, K., Li, W.Z., Lopez, R., Mcwilliam, H., Remmert, M., Soding, J., Thompson, J.D., Higgins, D.G., 2011. Fast, scalable generation of high-quality protein multiple sequence alignments using Clustal Omega. Mol. Syst. Biol. 7 https://doi.org/10.1038/msb.2011.75.
Sivaraman, J., Li, Y., Larocque, R., Schrag, J.D., Cygler, M., Matte, A., 2001. Crystal structure of histidinol phosphate aminotransferase (HisC) from Escherichia coli, and its covalent complex with pyridoxal-5'-phosphate and l-histidinol phosphate. J. Mol. Biol. 311, 761–776. https://doi.org/10.1006/jmbi.2001.4882.
Stepansky, A., Leustek, T., 2006. Histidine biosynthesis in plants. Amino Acids 30, 127–142. https://doi.org/10.1007/s00726-005-0247-0.
Sterling, T., Irwin, J.J., 2015. ZINC 15–Ligand discovery for everyone. J. Chem. Inf. Model. 55, 2324–2337. https://doi.org/10.1021/acs.jcim.5b00559.
Suzek, B.E., Wang, Y., Huang, H., Mcgarvey, P.B., Wu, C.H., Uniprot, C., 2015. UniRef clusters: a comprehensive and scalable alternative for improving sequence similarity searches. Bioinformatics 31, 926–932. https://doi.org/10.1093/bioinformatics/btu739.
The Uniprot, C., 2017. UniProt: the universal protein knowledgebase. Nucleic Acids Res. 45, D158–D169. https://doi.org/10.1093/nar/gkw1099.
Trott, O., Olson, A.J., 2010. AutoDock Vina: improving the speed and accuracy of docking with a new scoring function, efficient optimization, and multithreading. J. Comput. Chem. 31, 455–461. https://doi.org/10.1002/jcc.21334.
Vazquez, D.E., Balbuena, M.S., Chaves, F., Gora, J., Menzel, R., Farina, W.M., 2020. Sleep in honey bees is affected by the herbicide glyphosate. Sci. Rep. 10, 10516 https://doi.org/10.1038/s41598-020-67477-6.
Vernal, J., Cazzulo, J.J., Nowicki, C., 1998. Isolation and partial characterization of a broad specificity aminotransferase from Leishmania mexicana promastigotes. Mol. Biochem. Parasitol. 96, 83–92. https://doi.org/10.1016/S0166-6851(98)00117-0.
Vernal, J., Cazzulo, J.J., Nowicki, C., 2003. Cloning and heterologous expression of a broad specificity aminotransferase of Leishmania mexicana promastigotes. FEMS (Fed. Eur. Microbiol. Soc.) Microbiol. Lett. 229, 217–222. https://doi.org/10.1016/s0378-1097(03)00824-3.
Weidenmuller, A., Meltzer, A., Neupert, S., Schwarz, A., Kleineidam, C., 2022. Glyphosate impairs collective thermoregulation in bumblebees. Science 376, 1122–1126. https://doi.org/10.1126/science.abf7482.
Weigent, D.A., Nester, E.W., 1976. Purification and properties of two aromatic aminotransferases in Bacillus subtilis. J. Biol. Chem. 251, 6974–6980.
Wen, J., Nowicki, C., Blankenfeldt, W., 2015. Structural basis for the relaxed substrate selectivity of Leishmania mexicana broad specificity aminotransferase. Mol. Biochem. Parasitol. 202, 34–37. https://doi.org/10.1016/j.molbiopara.2015.09.007.
West-Roberts, J.A., Matheus-Carnevali, P.B., Schoelmerich, M.C., Al-Shayeb, B., Thomas, A.D., Sharrar, A., He, C., Chen, L.-X., Lavy, A., Keren, R., Amano, Y., Banfield, J.F., 2021. The Chloroflexi supergroup is metabolically diverse and representatives have novel genes for non-photosynthesis based CO2 fixation. bioRxiv. https://doi.org/10.1101/2021.08.23.457424.
Williams, C.J., Headd, J.J., Moriarty, N.W., Prisant, M.G., Videau, L.L., Deis, L.N., Verma, V., Keedy, D.A., Hintze, B.J., Chen, V.B., Jain, S., Lewis, S.M., Arendall 3rd, W.B., Snoeyink, J., Adams, P.D., Lovell, S.C., Richardson, J.S., Richardson, D.C., 2018. MolProbity: more and better reference data for improved all-atom structure validation. Protein Sci. 27, 293–315. https://doi.org/10.1002/pro.3330.
Witek, W., Sliwiak, J., Ruszkowski, M., 2021. Structural and mechanistic insights into the bifunctional HISN2 enzyme catalyzing the second and third steps of histidine biosynthesis in plants. Sci. Rep. 11, 9647. https://doi.org/10.1038/s41598-021-88920-2.

Yang, Z.F., Zhou, Y., Huang, J.L., Hu, Y.Y., Zhang, E.Y., Xie, Z.W., Ma, S.J., Gao, Y., Song, S., Xu, C.W., Liang, G.H., 2015. Ancient horizontal transfer of transaldolase-like protein gene and its role in plant vascular development. New Phytol. 206, 807–816. https://doi.org/10.1111/nph.13183.

Yue, J., Hu, X., Huang, J., 2013. Horizontal gene transfer in the innovation and adaptation of land plants. Plant Signal. Behav. 8, e24130 https://doi.org/10.4161/psb.24130.

Yue, J.P., Hu, X.Y., Sun, H., Yang, Y.P., Huang, J.L., 2012. Widespread impact of horizontal gene transfer on plant colonization of land. Nat. Commun. 3, 1152. https://doi.org/10.1038/ncomms2148.

Yuzawa, Y., Nishihara, H., Haraguchi, T., Masuda, S., Shimojima, M., Shimoyama, A., Yuasa, H., Okada, N., Ohta, H., 2012. Phylogeny of galactolipid synthase homologs together with their enzymatic analyses revealed a possible origin and divergence time for photosynthetic membrane biogenesis. DNA Res. 19, 91–102. https://doi.org/10.1093/dnares/dsr044.

Zallot, R., Oberg, N., Gerlt, J.A., 2019. The EFI web resource for genomic enzymology tools: leveraging protein, genome, and metagenome databases to discover novel enzymes and metabolic pathways. Biochemistry 58, 4169–4182. https://doi.org/10.1021/acs.biochem.9b00735.